

Hot subdwarfs in close binaries observed from space I: orbital, atmospheric, and absolute parameters and the nature of their companions

V. Schaffenroth¹, I. Pelisoli^{2,1}, B. N. Barlow³, S. Geier¹, and T. Kupfer⁴

¹ Institute for Physics and Astronomy, University of Potsdam, Karl-Liebknecht-Str. 24/25, 14476 Potsdam, Germany
e-mail: schaffenroth@astro.physik.uni-potsdam.de

² Department of Physics, University of Warwick, Gibet Hill Road, Coventry CV4 7AL, UK

³ Department of Physics and Astronomy, High Point University, High Point, NC 27268, USA

⁴ Department of Physics and Astronomy, Texas Tech University, PO Box 41051, Lubbock, TX 79409, USA

Received 08 June 2022/ Accepted 03 July 2022

ABSTRACT

Context. About a third of the hot subdwarfs of spectral type B (sdB), which are mostly core-helium burning objects on the extreme horizontal branch, are found in close binaries with cool, low-mass stellar, substellar, or white dwarf companions. They can show light variations due to different phenomena.

Aims. Many hot subdwarfs now have space-based light curves with high signal-to-noise ratio available. We used light curves from the Transiting Exoplanet Survey Satellite and the *K2* space mission to look for more sdB binaries. Their light curves can be used to study the hot subdwarf primaries and their companions and get orbital, atmospheric, and absolute parameters for those systems, when combined with other analysis methods.

Methods. By classifying the light variations and combining this with the fit of the spectral energy distribution, the distance derived by the parallaxes obtained by *Gaia* and the atmospheric parameters, mainly from the literature, we could derive the nature of the primary and secondary in 122 (75%) of the known sdB binaries and 82 newly found reflection effect systems. We derive absolute masses, radii, and luminosities for a total of 39 hot subdwarfs with cool, low-mass companions, as well 29 known and newly found sdBs with white dwarf companions.

Results. The mass distribution of hot subdwarfs with cool, low-mass stellar and substellar companions differs from those with white dwarf companions, implying they come from different populations. By comparing the period and minimum companion mass distributions, we find that the reflection effect systems all have M dwarf or brown dwarf companions, and that there seems to be several different populations of hot subdwarfs with white dwarf binaries — one with white dwarf minimum masses around $0.4 M_{\odot}$, one with longer periods and minimum companion masses up to $0.6 M_{\odot}$ and at the shortest period another with white dwarf minimum masses around $0.8 M_{\odot}$. We also derive the first orbital period distribution for hot subdwarfs with cool, low-mass stellar or substellar systems selected from light variations instead of radial velocity variations. It shows a narrower period distribution from 1.5 hours to 35 hours compared to the distribution of hot subdwarfs with white dwarfs, which ranges from 1 hour to 30 days. These period distributions can be used to constrain the previous common envelope phase.

Key words. binaries (including multiple): close; Stars: variables: general; subdwarfs; Stars: horizontal-branch; white dwarfs; Stars: low-mass; Stars: late-type; Stars: fundamental parameters

1. Introduction

Hot subdwarfs of spectral type O and B (sdO/Bs) are a mixture of different kinds of evolved stars located at or close to the bluest end of the horizontal branch, referred to as the extreme horizontal branch (EHB). Subdwarf O stars consist of many different objects including post-red giant branch and post-asymptotic giant branch stars. Most sdBs on the other hand, which are mostly found on the EHB, are core-He burning objects with very thin envelopes and masses close to the core-helium-flash mass of $0.47 M_{\odot}$ — for sdBs coming from low-mass star progenitors. A higher mass range of 0.35 - $0.65 M_{\odot}$ is possible for sdBs originating from more massive stars. A small fraction of sdBs is composed of extremely low-mass pre-white dwarfs (pre-ELM WD), which can cross the EHB on their way to the WD cooling track (Heber 2009, 2016). Significant mass-loss on the red giant branch (RGB) is necessary to form sdO/Bs, and Han et al. (2002,

2003) proposed different binary evolution channels to form such objects. Stable mass transfer leads to a composite sdB system with a K to F type companion and orbital periods of a few hundred days (Vos et al. 2018). They are double-lined binaries in the visible range showing spectral features from both the sdB and the cool companion. In the case of a larger mass ratio — above 1.2-1.5 — the mass-transfer is unstable and results in a common-envelope phase. The outcome of this poorly understood phase (Ivanova et al. 2013) is a sdB with a cool-low mass companion with a period of 0.05 day to around one day (Schaffenroth et al. 2019). Finally, after a stable mass transfer phase has passed, unstable mass-transfer can commence once the sdB's companion evolves into a red giant, leading to a short-period binary with a WD companion. He-core burning sdBs will evolve to sdOBs and sdOs after He-exhaustion in the core, before contracting onto the WD cooling track.

Most sdB binaries exhibit different kinds of variability in their light curves. Pelisoli et al. (2020) found that many of the composite sdB binaries show small amplitude variations in their light curves with periods of 0.5 d to a few days, due to spots on the companions. Subdwarf B stars with WD companions can show ellipsoidal deformation and even Doppler beaming in their light curves when the orbit is close enough and the WD massive enough (Kupfer et al. 2022, 2020a,b, 2017b). Systems with cool, low-mass companions show unique light curve variations resulting from the extreme temperature difference and small separation distance between the two stars (as small as $0.5 - 1 R_{\odot}$). The UV-bright hot subdwarf irradiates the side of the cool companion facing it, and this leads to hot and cold sides of the companion due to their being tidally locked. The irradiated face rotating in and out of view produces a quasi-sinusoidal flux variation called the reflection effect that exhibits broad minima and sharper maxima. In systems with inclination angles $\gtrsim 60 - 65^{\circ}$, eclipses can be observed given the right combination of stellar sizes and orbital separation. Such eclipsing sdB binaries are called HW Vir systems (e.g. Menzies & Marang 1986; Schaffenroth et al. 2019, 2021). Finally, some hot subdwarfs show variability due to short-period pulsations on the order of minutes (for sdO/B with $T_{\text{eff}} > 30000$ K) and long-period (for sdO/B with $T_{\text{eff}} < 30000$ K), low-amplitude pulsations on the order of hours (see Lynas-Gray 2021; Kupfer et al. 2019, for a summary). Some targets in binaries can even show variability due to both pulsations and binary effects (e.g. Vučković et al. 2007).

Geier et al. (2019) published a catalogue of 39 800 hot sub-luminous star candidates with $G < 19$ mag based on *Gaia* DR2 (Gaia Collaboration et al. 2018) colors, parallaxes, and proper motions and several ground-based, multi-band photometry surveys. They expect the majority of the candidates to be hot sdO or sdBs, followed by blue horizontal branch stars, hot post-AGB stars, and central stars of planetary nebulae (PN). The main purpose of their catalogue is to serve as a target list for current and future large-scale photometric and spectroscopic surveys.

One of those surveys is the *TESS* (Transiting Exoplanet Survey Satellite) mission (Ricker et al. 2015), which is observing over 90% of the northern and southern sky in different sectors. Each sector has a field of view of $24^{\circ} \times 90^{\circ}$ and is observed for 27 consecutive days, with a short break halfway through for data downlinking. The full frame images are downloaded every 30 min (and since sector 28, every 10 min), providing light curves of all stars in the field-of-view of 30 min (10 min) cadence. A number of pre-selected stars are downloaded every 2 min (since sector 28 some additionally also with 20s cadence). As members of the *TESS* Asteroseismic Consortium (TASC) Working Group (WG) 8 on compact pulsators with the subgroup WG8.4 on binaries, we were able to provide input target lists including bright hot subdwarfs from the hot sub-luminous star candidate catalogue (Geier et al. 2019), as well as with Guest Investigator programs G022141, G03221, and G04091 (PI: Brad Barlow). The majority of these targets were submitted because they either were known variable hot subdwarfs or were strong candidates for variability based off of their anomalous *Gaia* flux errors and other metrics (Barlow et al. 2022). This provides us with a few thousand space-quality light curves of hot subdwarf stars, including the few tens of light curves already obtained from *K2* (Howell et al. 2014) from different successful proposals. Consequently, we possess for the first time an expansive, high S/N data set of hot subdwarf light curves. Sahoo et al. (2020) and Baran et al. (2021b) used the 30 min cadence *TESS* light curves of observed targets from the hot sub-luminous star candidate catalogue (Geier et al.

Table 1: Result of our light curve search

| type | number (analyzed) |
|--|-------------------|
| new reflection effect systems | 82(0) |
| reflection effect systems with solved orbits | 20 (17) |
| HW Vir systems | 35 (0) |
| HW Vir system with solved orbits | 17 (17) |
| ellipsoidal deformation | 19 (11) |
| Doppler beaming | 16 (1) |

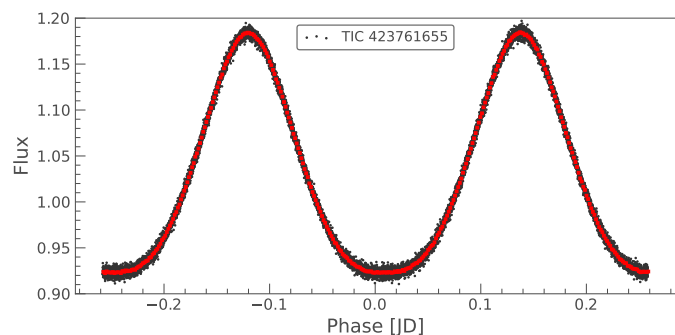


Fig. 1: Example *TESS* light curve of a reflection effect system (EC01578-1743). The light curve is shown phase-folded to the orbital period (black points) and also binned (red points).

2019) to search for light variations of hot subdwarf candidates and found several sdB+dM/BD candidates.

In this paper we present our search for hot subdwarfs with cool, low mass companions showing the reflection effect and hot subdwarfs with white dwarf companions showing ellipsoidal deformation and/or beaming, as well as a characterization of these systems. In section 2 we give more details to our target selection and our search for light variations. In section 3 we present our characterization of the primary star using the parallaxes and proper motions provided by *Gaia*, as well as the fit of the spectral energy distribution allowing us to get a mass distribution for the sdB in close binaries. In section 4 we show the distribution of the orbital parameters (period, semi-amplitude of the radial velocity curve) of our targets and compare the different populations. In section 5 we conclude and provide a short summary of our results.

2. Target selection and search for light variations

To look for reflection effect systems in the *TESS* light curves, we have searched *TESS* sectors 1-36 for variability in all stars brighter than $G < 16$ mag from the *Gaia* DR2 catalogue of hot sub-luminous stars (Geier et al. 2019), as well as the catalogue of spectroscopically confirmed hot subdwarf stars (in total 2883 targets with 2-min cadence light curves and 353 targets with 20-sec cadence light curves). (Geier 2020). We have used the light curves made available by the *TESS* Science Processing Operations Center (SPOC) through the Barbara A. Mikulski Archive for Space Telescopes MAST¹, using the PDCSAP flux, which corrects the simple aperture photometry (SAP) by removing instrumental trends, as well as contributions to the aperture expected to come from neighbouring stars other than the target of interest given a pre-search data conditioning (PDC). This is essential for *TESS*, as the pixel size is almost 21 arc sec. Through

¹ <https://mast.stsci.edu/>

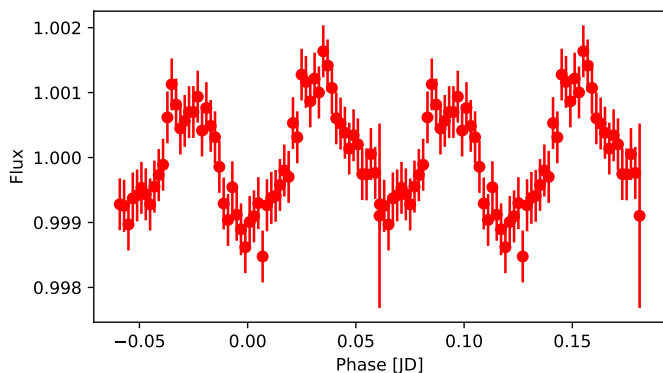


Fig. 2: Example *TESS* light curve of an ellipsoidal system (PG1043+760) showing additionally Doppler beaming. The light curve is shown phase-folded to the orbital period and binned.

the CROWDSAP parameter, the pipeline also provides an estimate of how much of the flux in the aperture belongs to the target. To avoid possible zero-point inconsistencies between different sectors, we divided the flux by the mean flux in each sector for each star.

We used the Python package *Astropy* (Astropy Collaboration et al. 2013, 2018) to calculate the Lomb-Scargle periodogram (Lomb 1976; Scargle 1982) of all light curves up to the Nyquist frequency, oversampling by a factor of 10. Light curves were then phase-folded to the period corresponding to the strongest peak, or twice this period for ellipsoidal systems, which have first harmonic peaks stronger than the fundamental orbital frequency. Our custom script that downloads the light curves and generates diagnostic plots with the periodogram and phase-folded light curves is publicly available². We visually inspected the diagnostic plots for all targets to confirm any variability and selected all objects showing a reflection effect (with and without eclipses), as well as stars showing ellipsoidal deformation. All targets with confirmed light variations can be found in Table A.4.

Additionally, we inspected the *TESS* or *K2* light curves of all hot subdwarfs with with orbits characterized by radial velocity measurements (Kupfer et al. 2015, and references in Table A.4). All light curves were downloaded, phase-folded to the orbital period, and binned using the Python package *LIGHTKURVE* (Lightkurve Collaboration et al. 2018)³. We computed the periodogram around the orbital period to search for any small peaks resulting from weak reflection or ellipsoidal deformation signals. For targets without any variations, we phase-folded the light curve to the orbital period derived by time-resolved spectroscopy and determined the signal-to-noise ratio. The results of our search are shown in Table 1, A.3, and A.4. Example *TESS* light curves of a reflection effect system and an ellipsoidal system additional showing Doppler beaming can be found in Fig. 1 and 2. The complete set of light curves, along with full details regarding our modeling and analysis methods, will be presented in an additional paper (Paper II, Schaffenroth et al. in prep.).

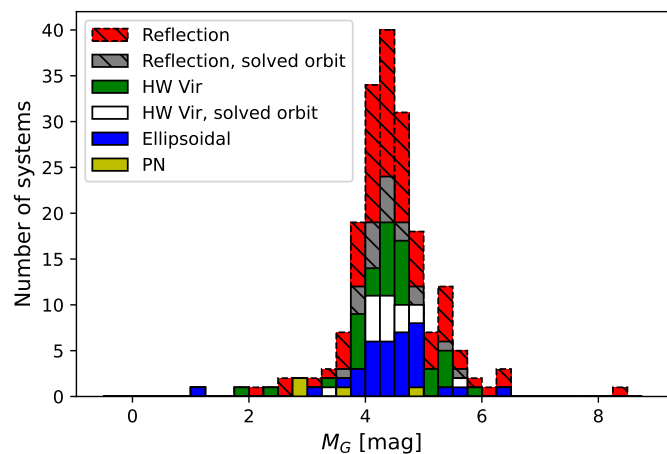


Fig. 3: *Gaia* absolute magnitude M_G of all our targets divided into different groups according to the different light curve variations they show as shown in the legend.

3. Characterizing the primary star

3.1. Absolute magnitude and reduced proper motion

3.1.1. Method

Both hot subdwarf and hot WD binaries containing a cool, low-mass companions can show a reflection effect (Schaffenroth et al. 2019), as can some sOs that are central stars of planetary nebula (CSPN). In order to determine the true nature of the primary star, we used the colors, parallaxes, and proper motion from *Gaia* EDR3 (Gaia Collaboration et al. 2021), as was done in Schaffenroth et al. (2019) for newly discovered HW Vir systems. Using the *Gaia* G magnitude together with the parallax, we could determine the absolute magnitude of our targets using the distance modulus ($G - M_G = 5 \log_{10} d - 5$). We ensured that all of our targets but one (which we identified as a potential triple system) had a small uncertainty in their parallax ($\lesssim 10\%$) and a Renormalised Unit Weight Error (RUWE) below 1.4 (e.g., Penoyre et al. 2022). A higher RUWE indicates potential problems with the parallax.

Another way to confirm our target selection is to determine the reduced proper motions $H_G = G + 5(\log \mu + 1)$. Stars that are farther away should show less transverse velocity on average than those that are closer, and the reduced proper motion is therefore a proxy for the distance; closer objects should have larger reduced proper motions. Typically, hot subdwarfs show reduced proper motions between 5 and 14 mag (e.g. Schaffenroth et al. 2019).

3.1.2. Results

The results are found in Table A.4. Inspecting the absolute magnitude M_G distribution of all our targets (Fig. 3), we see that it peaks around $M_G = 4.5$, as expected for hot subdwarf stars (Geier 2020). We have only one target with $M_G > 7$ mag, which is most likely a WD primary. We also have some targets with $M_G < 3$ mag, which are known CSPN, or pre-ELM WD.

Our reduced proper motion distribution shown in Fig. 4 also confirms that our targets are most likely hot subdwarf stars.

Since hot subdwarfs are of spectral type O and B, they have temperatures between 25 000 to 50 000 K and blue colors. Their luminosities are lower than main sequence stars and higher than

² <https://github.com/ipelisol/TESS-LS>

³ <https://docs.lightkurve.org>

⁴ <https://stilism.obspm.fr/>

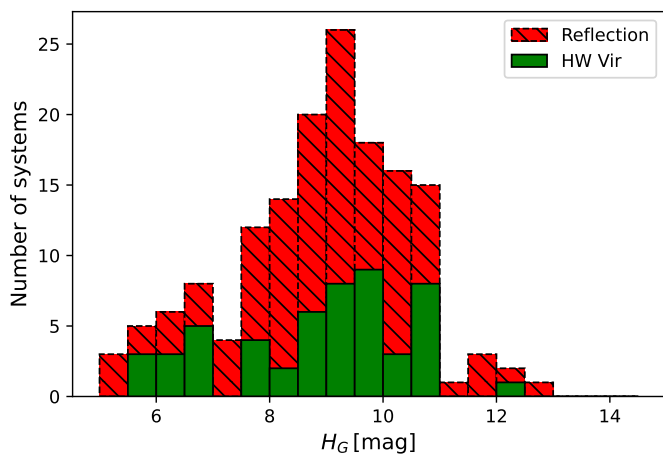


Fig. 4: Reduced proper motion of all our reflection effect systems (eclipsing and non-eclipsing).

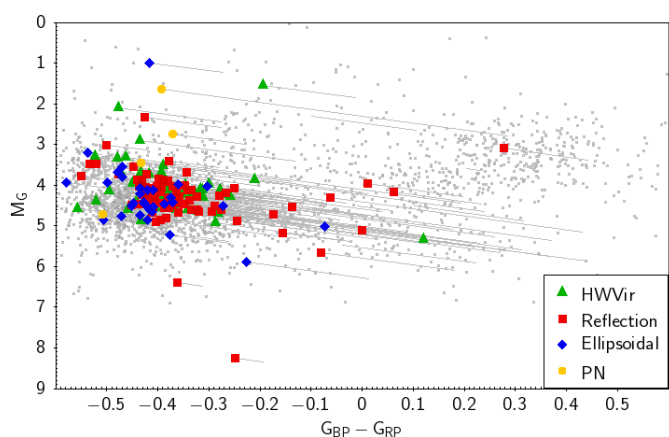


Fig. 5: $G_{BP} - G_{RP}$ vs M_G diagram. The targets are again grouped according to their light variations. All targets have been corrected for interstellar extinction using Stilism⁴. The correction is shown with the grey lines. In comparison the known sdO/Bs taken from Geier (2020) are shown with the grey data points.

hot white dwarfs. To check where we find our targets in the color-magnitude diagram, we plot a $G_{BP} - G_{RP}$ vs M_G diagram (see Fig. 5). Both the absolute magnitude and $G_{BP} - G_{RP}$ color were corrected for interstellar extinction using 3D maps (Lallement et al. 2014; Capitanio et al. 2017). Our targets are located at $-0.5 < G_{BP} - G_{RP} < 0.3$, with most of the targets clustering at $G_{BP} - G_{RP} < -0.25$. There is a slight trend that targets with $G_{BP} - G_{RP} > -0.25$ seem to have smaller M_G . As all of those targets show a high extinction, this trend can most likely be explained by insufficient correction of the interstellar extinction. The distribution of our targets on the sky (Fig. 6) shows that most of the targets with high extinction are found close to the galactic plane, up to $\pm 20^\circ$ away. The comparison with the known sdO/Bs from Geier (2020) shows quite a good agreement. One target is found with $G_{BP} - G_{RP} = 0.3$ at an absolute magnitude $M_G = 3$, consistent with known composite sdB stars. Only a few of our targets are found at $G_{BP} - G_{RP} < -0.45$, which is probably due to the fact that most of them are cooler helium-core burning sdB stars rather than evolved sdO stars. The comparison of the position of all our targets grouped together by the observed light variations (Fig. 7) shows that all different target types seem to be equally distributed on the sky.

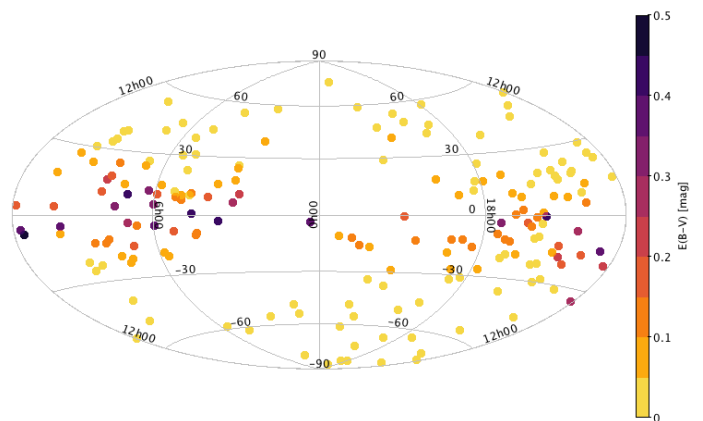


Fig. 6: Position of our targets on the sky (in galactic coordinates). The color coding is giving by the color excess $E(B-V)$.

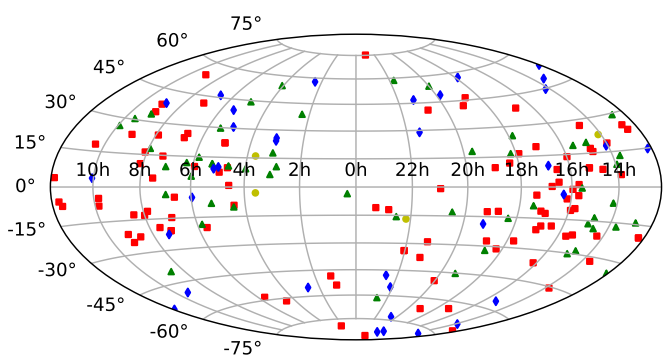


Fig. 7: Comparison of the position of our targets on the sky (in galactic coordinates). The green triangles mark HW Virs, the red squares reflection effect systems and the blue diamonds ellipsoidal systems, and the yellow circles CSPNs.

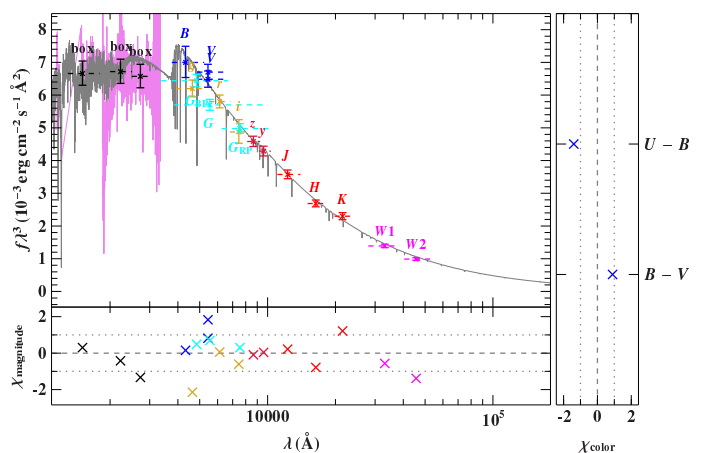


Fig. 8: Example of an SED fit (for the sdB+WD system PG1519+640).

3.2. Spectral energy distribution

3.2.1. Method

To confirm a candidate's status as a hot subdwarf, we need to derive the effective temperature T_{eff} and surface gravity $\log g$. The best way to determine atmospheric parameters is to observe and model the target's spectrum. However, it is also possible to

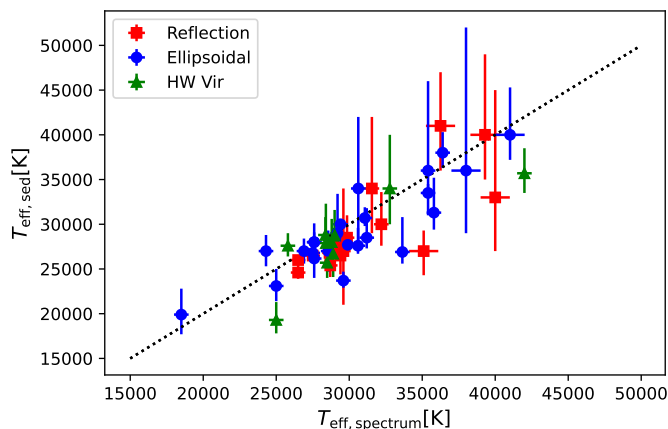


Fig. 9: Comparison of the effective temperature determined by spectral fitting and spectral energy distribution fitting. Blue circles mark systems showing ellipsoidal deformation, green triangles mark HW Vir systems and red squares mark reflection effect systems.

determine T_{eff} , as well as the radius and the luminosity, by fitting the spectral energy distribution (SED) with synthetic spectra and combining this with the distance from the *Gaia* parallax (see Heber et al. 2018; Irrgang et al. 2021, for more details on this method). The shape of the SED gives us T_{eff} as well as the interstellar reddening. And by comparing the observed and synthetic flux $f(\lambda)$ and $F(\lambda)$ respectively, we can derive the angular diameter $\theta = 0.5 \sqrt{\frac{f(\lambda)}{F(\lambda)}}$, which can be used to derive the radius $R = \theta/(2\varpi)$ and the luminosity $L/L_{\odot} = (R/R_{\odot})^2(T_{\text{eff}}/T_{\text{eff},\odot})^4$ by using the *Gaia* parallax ϖ and parallax offset.

Using the $\log g$ determined by the spectral fitting and the radius determined by the SED and *Gaia* distance, we can also derive the mass of the hot subdwarf $M = gR^2/G$ for the hot subdwarf binaries with known atmospheric parameters.

3.2.2. Results

One example SED fit is shown in Fig. 8. Unfortunately, the SED fitting is not straightforward for the reflection effect systems since our targets show light variations and the photometry we used from the literature was taken at a random phase.

In light of the above, we tested our method on reflection effect and ellipsoidal systems with known atmospheric parameters and sufficient photometric data (see Table A.1 for the results). The comparison between effective temperatures determined by spectral fitting and spectral energy distribution fitting (Fig. 9) shows that for systems with $T_{\text{eff}} \lesssim 32000$ K, the fitting of the SED can determine the T_{eff} very well if we neglect infrared photometry, since the contribution of the companion gets larger there. UV (IUE or *Galex* FUV or NUV) and SDSS u' photometry are essential for disentangling the effect of T_{eff} and interstellar reddening on the SED by covering the Balmer jump, so we exclude all targets without sufficient UV photometry from the SED fitting. For hotter systems, we see a larger scatter. For $T_{\text{eff}} > 42000$ K the Balmer jump is not visible anymore, and so the temperature cannot be derived anymore without constraining the interstellar reddening. There is also a slight tendency that the SED fitting derives smaller temperatures than the spectral fitting.

Using the derived luminosities, we construct a Hertzsprung-Russell diagram for reflection effect and ellipsoidal systems with

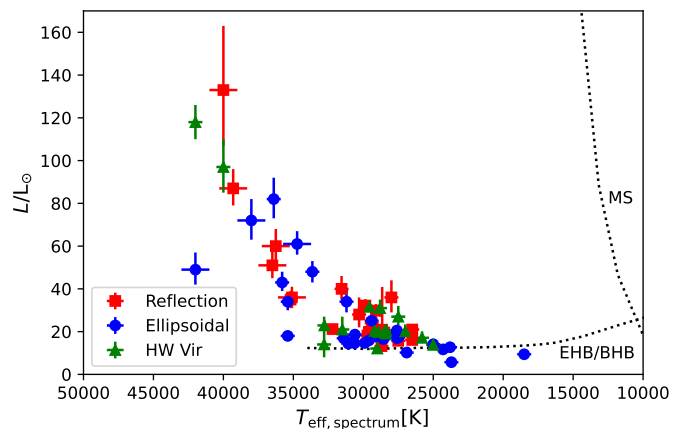


Fig. 10: Hertzsprung-Russell diagram of our targets with known atmospheric parameters. Blue circles mark systems showing ellipsoidal deformation, green triangles mark HW Vir systems and red squares mark reflection effect systems. The dotted lines mark the zero-age main sequence or EHB/BHB.

spectroscopic parameters for the first time. This is shown in Fig. 10. The sdBs on the EHB with temperatures below 33000 K are found at similar luminosities between 15 and 40 L_{\odot} . At larger temperatures the luminosity increases with the temperature but also a larger scatter is visible resulting from larger differences in the radii. Németh et al. (2012) showed that the He abundances and the difference in He abundance increases with the temperature. The larger scatter of the radii and hence the luminosity at larger temperatures may be related to those He abundance differences.

With the spectroscopic $\log g$ and the radius from the SED fitting, we were able to derive the mass distribution of reflection effect, HW Vir and ellipsoidal systems. A similar approach was used in Krzesinski & Balona 2022, which derived the mass distribution of pulsating hot subdwarf candidates with spectroscopic parameters to be a broad peak with the maximum at 0.45 M_{\odot} . However, they state that their analysis might not be reliable and useful to derive masses of single systems.

Our result is shown in Fig. 11, 12 and 13 and Table A.1. For the HW Vir systems, we derive a mass of $0.46^{+0.08}_{-0.12} M_{\odot}$ using a skewed normal distribution. As the typical mass error is about 0.05 M_{\odot} this suggests an intrinsically broader peak. The non-eclipsing reflection effect systems seem to have a broader peak with more higher-mass sdBs. As the only difference compared to the HW Vir systems is that they have no eclipses, we would not expect any difference. Determining atmospheric parameters from reflection effect systems has to be done with caution, as the contribution of the companion to the total flux changes with the orbital phase causing the reflection effect. So the atmospheric parameters have to be determined at or close to phase zero, when only the cool side of the companion is visible, or at the secondary eclipse, when the companion is occulted by the sdB in an eclipsing system. Most of the atmospheric parameters of the reflection effect systems have been determined from a single spectrum or co-added spectra at different orbital phases, causing systematic shifts to higher temperatures and higher $\log g$. This influences the determination of the radius and will result in a shifted mass. The HW Vir systems have been studied much more carefully, and so their determined atmospheric parameters are much more reliable.

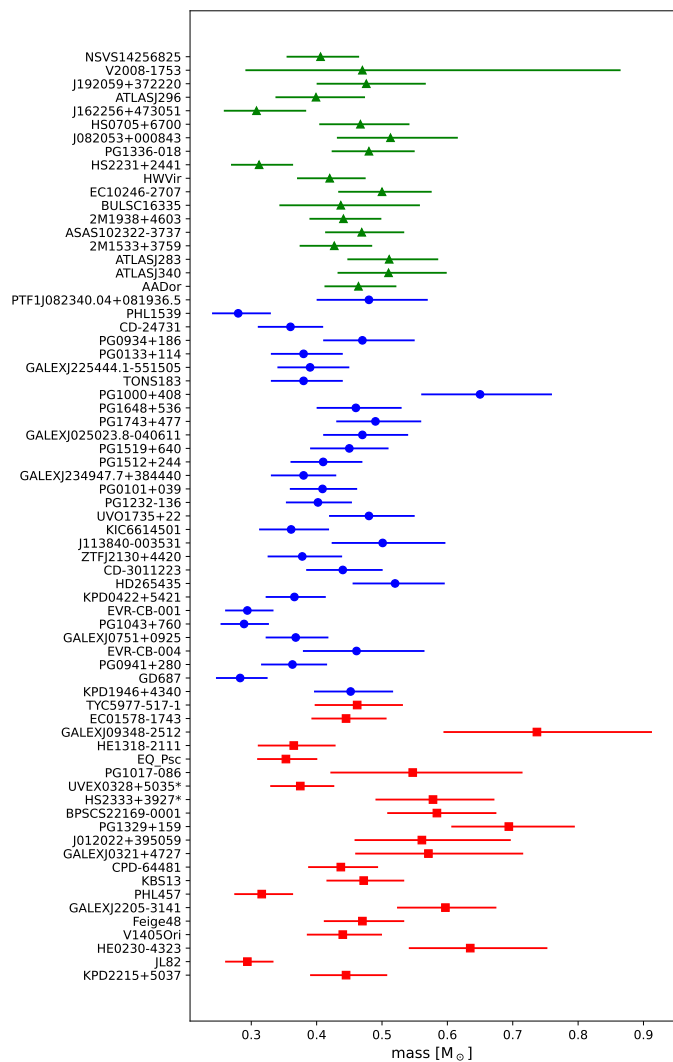


Fig. 11: Masses determined by combining the spectroscopic analysis with the fit of the SED and the *Gaia* parallaxes. Blue symbols mark systems showing ellipsoidal deformation, green symbols mark HW Vir systems and red symbols mark reflection effect systems.

The masses of the sDBs with white dwarf companions show a distribution with a similar width but a peak shifted to lower masses at $0.38^{+0.12}_{-0.08} M_{\odot}$. The distribution also seems to be slightly asymmetric, extending to higher masses. The cumulative distribution shows the shift in mass more clearly, and shows that it is indeed significant.

The samples were taken from the literature and are not complete but are suffering from selection effects, which are not easy to determine. However, in the *Gaia* color-magnitude diagram (Figure. 5) and the sky distribution (Fig. 7), we can see that sDB+WD and the sDB+dM populations are overlapping well. The sDBs in the systems of both populations have been identified the same way by color selection. Hence, we expect that the selection effects should be similar for both populations and that they are comparable nevertheless.

The sDB+WD systems have been found preferably by RV variations in contrast to the HW Vir systems, as the sDB+WD systems show much smaller light variations. Both samples included only systems at the short period end of their period distribution (see Table A.4). A larger sample over a larger period

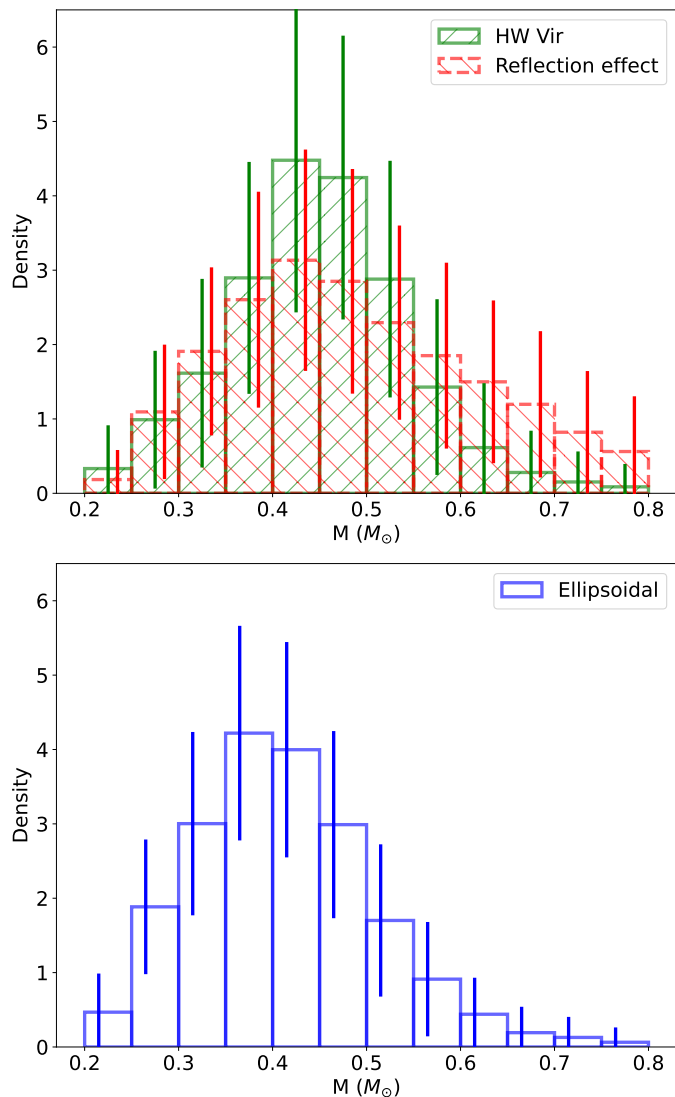


Fig. 12: Histogram of the masses determined by combining the spectroscopic analysis with the fit of the SED and the *Gaia* parallaxes.

range for both populations will be necessary to confirm our findings and also find or exclude differences of the sDB mass in systems with different orbital periods.

By fitting the SED and combining this with the *Gaia* parallaxes we can also constrain the atmospheric parameters of our reflection effect candidates, which do not have spectroscopic parameters, by fitting the SED and assuming a canonical mass for the sDB. From the radius we derive, we can constrain the $\log g$ in this way and constrain the atmospheric parameters for 44 targets with sufficient UV photometry. The results can be found in Table A.2. The atmospheric parameters are compared to the solved systems in the $T_{\text{eff}} - \log g$ diagram (Fig. 14). This shows that our reflection effect candidate systems are mostly found on the EHB. Some of the candidates are on post-EHB tracks, which means the He in the core was exhausted and they are evolving away from the EHB. Only one candidate was found above the EHB, which could be a lower mass pre-He WD.

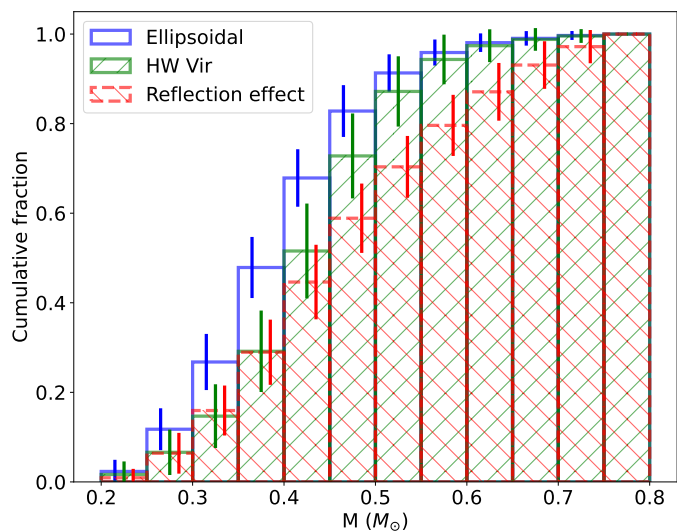


Fig. 13: Cumulative distribution of the masses determined by combining the spectroscopic analysis with the fit of the SED and the *Gaia* parallaxes.

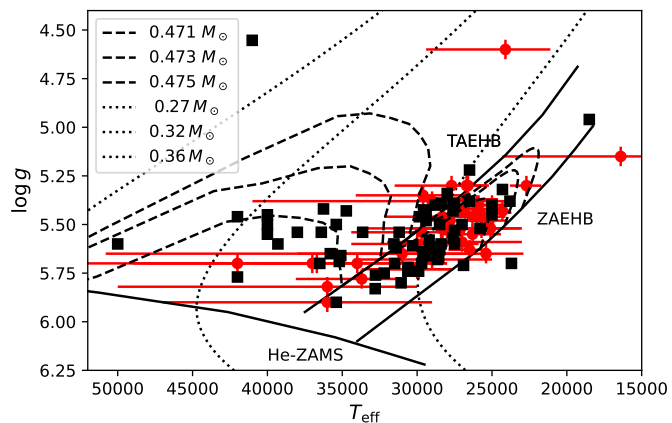


Fig. 14: $T_{\text{eff}} - \log g$ diagram of the sdB binaries with spectroscopic parameters (black squares) compared to the reflection effect candidates (red diamonds). The black solid lines mark the zero-age extreme horizontal branch (ZAEHB), the terminal-age extreme horizontal branch (TAEHB) and the He-main sequence (He ZAMS). The dashed lines are evolutionary tracks by Dorman et al. (1993) for sdB masses of 0.471, 0.473, and 0.475 M_{\odot} . The dotted lines are tracks for extremely low mass white dwarfs of a mass of 0.27, 0.32, and 0.36 M_{\odot} by Althaus et al. (2013).

4. The period distribution from light variations found by TESS

4.1. The selection effects of TESS

In order to judge the completeness of our reflection effect sample, we simulated the expected amplitude of the reflection effect for a typical sdB+dM system with different orbital periods and compared this to the noise level of the *TESS* satellite for stars of different brightness (see Fig. 15). This was done by checking the noise level in the light curves of different sdB stars of the same brightness not showing any variations in the light curve. For a 15 mag system, the detection limit is about 0.3%. As expected, the amplitude of the variations decreases with lower in-

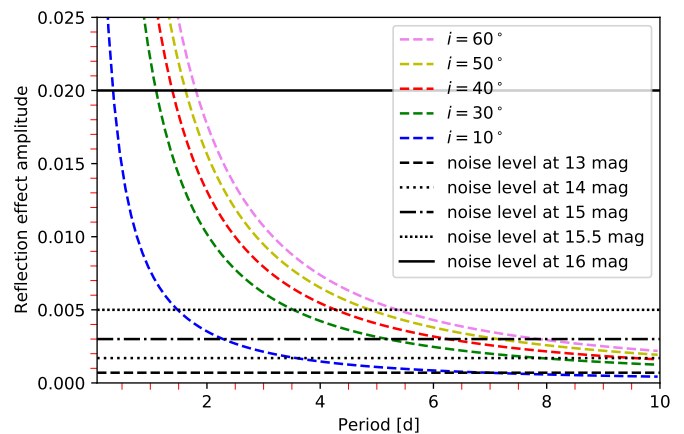


Fig. 15: Amplitude of the reflection effect of a typical sdB+dM system for different periods and inclinations. The black lines mark the *TESS* noise level for stars of different brightness.

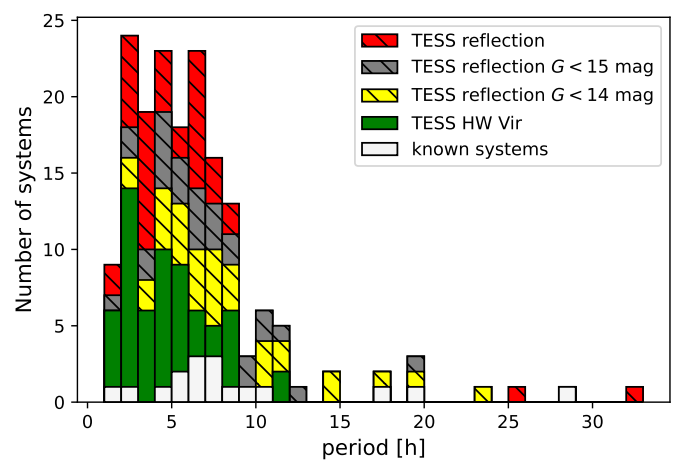


Fig. 16: Period distribution of the reflection effect systems with and without eclipses observed by *TESS*. The known reflection effect systems are marked in white, the eclipsing reflection effect systems are marked in red, and the reflection effect systems without eclipses are marked in yellow, green and grey for systems with $G < 13$ mag, $G < 14$ mag and all other systems respectively.

clination. But even with a low inclination of only 10° , we would expect to detect the reflection effect for a system brighter than 15 mag with *TESS* up to two days, for higher inclinations of about 40° up to about 6 days, and in inclinations of more than 60° up to 8 days. Since the reflection effect becomes more sinusoidal at low inclinations, it is quite hard to distinguish it from other variations like pulsations or spots. Consequently, we will probably find low-inclination reflection effects only for the systems in which the period is already known from the RV curve. But the inclination should correlate with the period, and so this should not influence the period distribution we derive.

Another selection effect could come from *TESS* having such large pixels (21 arc-sec per pixel). If another star of comparable or higher brightness is close to the star, the light curve can become contaminated. *TESS* tries to correct for this additional flux through its reported PDCSAP flux, and it uses the CROWDSAP keyword in the header to quantify the contamination level. This correction can over- or underestimate the flux, and so the am-

plitude is not entirely reliable when a bright star is so close and it contributes significantly to the flux in the target pixel. This means that we might miss some reflection effect systems when unrelated stars are too close, but overall this correction seems to be quite good (a few percent difference; see Paper II for more details) and there is no reason why this should influence the period distribution of the detected systems.

As the amplitude of the ellipsoidal modulation is much smaller as can be seen in Fig. 2, this is very different for sdB+WD systems because we will only find the systems with the closest periods and/or highest mass companions by our light variation search, if the period is not known by RV variations for example.

4.2. Period distribution of the reflection effect systems

Taking all of this into account, we will never acquire a *complete* sample of reflection effect binaries from light curves alone, and the situation is even worse for the ellipsoidal systems. We do expect to find most reflection systems with higher inclinations observed by TESS up to periods around 7 days, as they can be identified from their light curve shapes with ease. Fig. 16 presents our observed orbital period distribution for sdBs with cool, low-mass companions. To ensure we do not see any difference with the brightness, we also checked the distributions of reflection effect systems of different brightness with a two-sample Kolmogorov–Smirnov test, but we could not find any significant differences. The period distribution shows that the reflection effect systems without eclipses tend to be found at periods longer than the eclipsing systems. This is expected as the eclipse probability decreases quickly with increasing separation distance and period. The period distribution shows a broad peak from 2–8 hours and falls off quickly on either end. There are very few systems with periods shorter than 2 hours, and none are below 1.2 hours. Above 8 hours, the distribution falls off quickly, and only a handful of systems are found beyond 20 hours. Despite our ability to detect systems with periods up to several days, the longest-period system we have found has a period of 35 hours. Since we do not find any longer-period systems, they either do not exist, or they are incredibly rare. As *TESS* continues to observe more and more reflection effect systems and increase the sample size, hopefully this question can be answered.

5. The companions of the close sdB binaries with solved radial velocity curves

5.1. The nature of the companion

As we have seen, the reflection effect generates a flux variation that is detectable at periods up to several days. The light variation from ellipsoidal deformation or Doppler beaming, however, is much weaker on average (below 0.1–0.2%) at periods up to about one day and not detectable at longer periods. We can use these facts to differentiate between cool, low-mass companions and white dwarf companions (more details and the analysis of those systems is shown in Paper II) for the systems with periods known from RV variations.

We phased the available light curves of all hot subdwarfs with solved orbits (135 of the 165 systems have Kepler or *TESS* light curves). Of those, 40 show a reflection effect and 33 show ellipsoidal deformation or Doppler beaming indicating that they have a white dwarf companion (see Paper II for more details). The rest do not show significant variations at the orbital period. We derived the signal-to-noise ratio for all light curves not exhibiting any variations. The result can be found in Table A.3.

To constrain the nature of the companion, we used the amplitude estimates at a given period and inclination shown in Fig. 15. Under the assumption all orbital plane orientations are equally probable, the probability of the inclination being lower than 10° is only $1 - \cos 10^\circ = 1.5\%$ (Gray 2005). Therefore, we classify as sdB+WD systems all sdB binaries with light curves having a signal-to-noise ratio smaller than the amplitude expected for a reflection effect system observed at an inclination angle $< 10^\circ$ (probability $> 98.5\%$).

Moreover, for companion masses larger than $0.45 M_\odot$ we would expect to see an infrared excess in the SED, if the companion would be a main sequence companion. Therefore, we also classify all sdB binaries with minimum companion masses $> 0.45 M_\odot$ as sdB+WD system. The minimum companion masses can be derived by the mass function

$$f(M_1, M_2) = \frac{M_2^3 \sin^3 i}{(M_1 + M_2)^2} = \frac{PK_1^3}{2\pi G}, \quad (1)$$

assuming a mass of $0.47 M_\odot$ for the sdB and an inclination of 90° . We are unable to constrain the nature of the companion in this way for only 12 of our systems, as the noise in their light curves is too large and the minimum companion mass is too small. In total, this gives us 83 sdB+WD systems and allows us to constrain the nature of 75% of all close sdB binaries with solved orbits.

Most of the sdB binaries with solved orbits have been detected by radial velocity variations, a method biased towards shorter periods, higher companion masses, and higher inclinations. Only very few of these were found by light variations. In this sample, about one-third of the sdB binaries have M dwarf or brown dwarf companions, and two-thirds have white dwarf companions.

5.2. The period distributions

The updated period distributions of the dM/BD and WD companions and their differences are also interesting, as shown in Fig. 17. We already discussed the distribution of the reflection effect and HW Vir systems showing periods from 2 hours to about 1 day. The systems with WD companions, on the other hand, show a broad distribution from just about one hour to 27 d. On top of this broad distribution we find two distinct peaks at around one day and around 5–10 days. The companion is still undefined only for a small number of systems. Most of them have periods longer than one day, agreeing well with the distribution of the WD companions, so it is likely they are also sdB+WD systems.

5.3. The minimum companion masses

To get a clearer picture of the masses of the close companions to hot subdwarf stars, we update the plot of RV semi-amplitude versus orbital period for all known sdB binaries (as shown in Kupfer et al. 2015) with spectroscopic solutions and with *TESS* or Kepler light curves (Fig. 18) as well as plot the minimum companion mass distribution in Fig. 19.

Our new sample adds many more systems with companion mass constraints to this plot. As we have seen, it is possible to constrain the minimum mass of the companion from the RV semi-amplitude of the sdB and the orbital period, when assuming a mass for the sdB. This is given by the black lines for different periods. For a random distribution of system angles, the probability to have a system with inclination $> 60^\circ$ is the same as

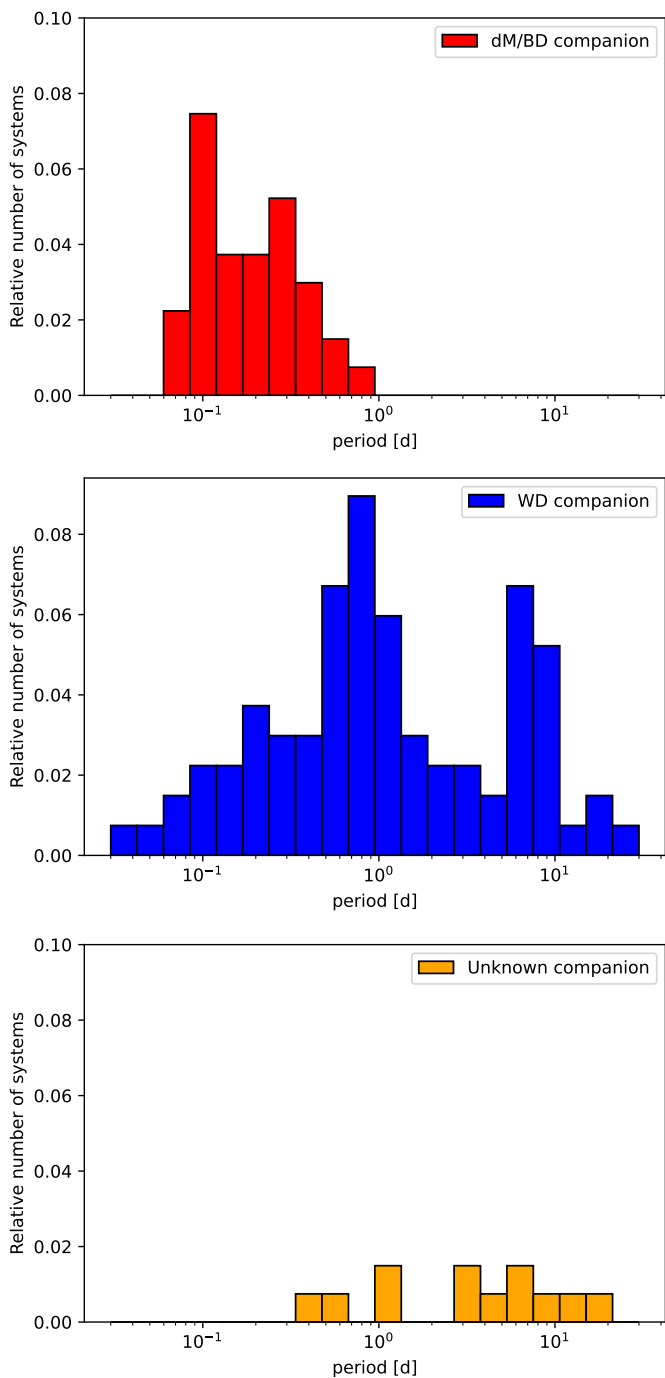


Fig. 17: Period distribution of the hot subdwarf binaries with solved orbits with dM/BD companions in the top panel, with WD companions in the middle and unknown companions in the lower panel.

for an inclination of $< 60^\circ$, and so about half of the companions should have masses of only up to 20% higher than the minimum companion mass.

We find that systems with cool, low-mass companions cluster around the hydrogen-burning limit with masses up to $0.25 M_\odot$ with one exception. The white dwarf companions to sdB stars have higher minimum masses, and it looks like there are three different populations. At the shortest periods from approximately one to about three hours, a small group of WD companions with minimum companion masses around 0.7 to $0.8 M_\odot$ are

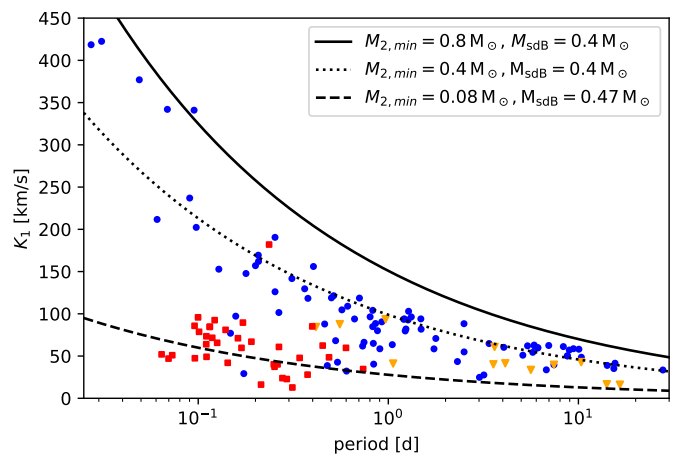


Fig. 18: RV semi-amplitudes of all known short-period sdB binaries with spectroscopic solutions and with *TESS* or *Kepler* light curves plotted against their orbital periods (red squares: dM/BD companions, blue circles: WD companions, yellow diamonds: unknown type). The lines mark a certain minimum companion mass derived from the binary mass function (assuming 0.47 or $0.4 M_\odot$ for the sdBs).

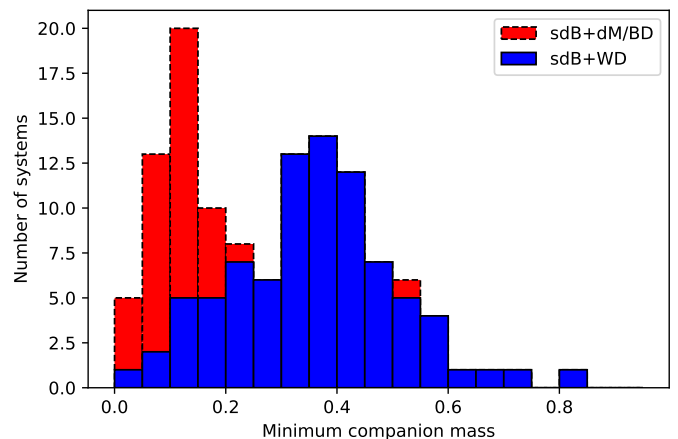


Fig. 19: Minimum companion mass distribution of all known short-period sdB binaries with spectroscopic solutions and with *TESS* or *K2* light curves (assuming $0.47 M_\odot$ for a sdB with dM/BD companion or $0.4 M_\odot$ for a sdB with WD companion).

found. Most of the WD companions are found in binaries with longer periods. Up to a period of about 4 days they seem to have significantly lower minimum companion masses with a mass ratio close to one (around $0.4 M_\odot$, when assuming an sdB mass of $0.4 M_\odot$). Systems with periods belonging to the second peak in the period distribution around 5-10 days show some indication of slightly higher minimum companion masses above $0.4 M_\odot$ up to $0.6 M_\odot$.

6. Discussion and Conclusions

Our light variation search increases the number of known reflection effect systems from 19 to 104 systems. Moreover, we detected 23 new sdB+WD systems showing tiny variations with amplitudes below $\sim 0.1\%$, due to Doppler beaming or ellipsoidal deformation in their light curves.

Table 2: Masses of the solved sdB+WD systems derived by light curve analysis and SED fitting

| target | $M_{\text{sdb,SED}}$ [M_{\odot}] | $M_{\text{sdb,lc}}$ [M_{\odot}] | references |
|----------------|---|--|-------------------------|
| KPD1946+4340 | $0.452^{+0.065}_{-0.056}$ | $0.47^{+0.03}_{-0.03}$ | Bloemen et al. (2011) |
| CD-3011223 | $0.44^{+0.061}_{-0.056}$ | $0.47^{+0.03}_{-0.03}$ | Geier et al. (2013) |
| PTF1J0823+0819 | $0.48^{+0.09}_{-0.08}$ | $0.45^{+0.09}_{-0.07}$ | Kupfer et al. (2017b) |
| EVR-CB-001 | $0.294^{+0.04}_{-0.034}$ | $0.21^{+0.05}_{-0.05}$ | Ratzloff et al. (2019) |
| EVR-CB-004 | $0.461^{+0.104}_{-0.087}$ | $0.52^{+0.04}_{-0.04}$ | Ratzloff et al. (2020b) |
| ZTFJ2130+4420 | $0.378^{+0.061}_{-0.053}$ | $0.337^{+0.015}_{-0.015}$ | Kupfer et al. (2020b) |
| HD265435 | $0.59^{+0.17}_{-0.14}$ | $0.64^{+0.10}_{-0.09}$ | Pelisoli et al. (2021) |

The characterization of the reflection effect systems in our sample shows that all except one have hot subdwarf primaries. The one exception was a system with a white dwarf primary. Similar results were found in other surveys, such as EREBOS (Schaffenroth et al. 2019). The detection of a white dwarf primary is not a complete surprise since we selected targets from the *Gaia* DR2 catalogue of hot subluminescent stars, which does have some overlap with the white dwarf catalogue. Nonetheless, most of the primaries in our systems should be sdO/B stars. The reflection effect is only visible in hot white dwarfs, which are much rarer. Moreover, white dwarfs are much fainter than hot subdwarf stars. And since sdBs are mainly formed by binary evolution, the binarity rate of sdBs is much higher than of WDs. That is why reflection effect systems with hot subdwarf primaries will dominate all surveys for reflection effect systems.

To check the mass determination of the sdB using the SED and the *Gaia* parallaxes, we compared the masses derived by this method with the masses derived by the light curve analysis of several ellipsoidal systems. This is shown in Table 2. The masses derived by the two different methods agree very well within the errors for all systems, thereby showing the validity of our spectrophotometric *Gaia* distance method.

The comparison of the mass distribution of the sdB+dM and the sdB+WD (Fig. 12) shows that they differ significantly. The mass distribution of sdBs with WD companions is shifted to lower masses compared to sdBs with dM/BD companions. This implies that sdBs with dM/BD companions come from a different population than sdBs with WD companions. The sdB+dM systems show a peak around the canonical mass for He burning and a few systems at higher and lower mass, as predicted by binary population synthesis models (Han et al. 2002, 2003). Those non-canonical systems can originate from young, higher-mass systems igniting He in the core under non-degenerate conditions or be pre-He WDs not massive enough for He-burning that are passing through the sdB region in the HRD. The sdB+WDs, on the other hand, show many more low-mass systems. The sdB binaries with massive companions are observed towards the Galactic plane, where younger stars are found. This indicates that those systems are preferably formed in younger populations than the sdB+dM stars. The other sdB+WD systems seem to be equally distributed on the sky (see Fig. 7).

The observation of space-based, high S/N light curves covering a time span of at least 27 days up to several months of so many sdBs gave us for the first time a large sample of reflection effect binaries. Since they were selected mainly from the *Gaia* hot subdwarf catalogue and had no prior RV measurements, this gives us the first period distribution of sdB+dM systems selected *only* by light variations. The orbital period distribution of post-CE binaries is mainly dependent on the criterion for the ejection

of the CE (Han et al. 2002), and so this distribution can be used to constrain the common-envelope phase when combined with the companion mass distribution as done in Ge et al. (2022) for the sample of hot subdwarf binaries from Kupfer et al. (2015) or comparing it to a modelled sdB binary sample using binary population synthesis.

Aided by high-quality *TESS* light curves, we could constrain the nature of the companion in 75% of the sdB binaries with solved orbits and compare them. As seen in Fig. 17, the period distribution of the sdB+dM systems is concentrated in a much smaller period range compared to the sdB+WD systems, which are found over a wide range of periods from 0.03-30 days. The distribution of the minimum companion masses found at a certain orbital period (Fig. 18) shows that the companions in the reflection effect systems have minimum masses typical for BD/dM systems ($0.05 - 0.2 M_{\odot}$). There is no change with the orbital period visible. For the sdB+WD systems this is different. There seem to be two distinct groups of companion masses. At the shortest periods below 0.1 d, WD companions with high minimum masses around $0.8 M_{\odot}$ are found, which could be CO or ONe WDs. At longer periods, the WD companions seem to have significantly lower minimum masses, with masses around $0.4 M_{\odot}$. Many of those could be He-WD companions. At the longest periods the masses seem to be slightly higher indicating a third population of low-mass CO WD companions. This could suggest that sdB+WD systems at the shortest periods come from a different population with higher-mass progenitors having higher-mass companions than the longer period sdB+WD systems, which is consistent with predictions by binary population synthesis (Han et al. 2002, 2003).

The high signal-to-noise light curves allowed us to derive parameters for a large number of sdB+dM/BD and sdB+WD systems. Details of this light curve modeling and analysis are discussed in a separate paper (Paper II).

As *TESS* continues to observe, the number of high-quality reflection effect and sdB+WD light curves will continue to grow. This will further increase our sample size and improve constraints on the mass and period distributions. Future spectroscopic and photometric surveys like 4MOST, BlackGem, and Vera Rubin Observatory will also increase our sample size and our knowledge about these systems.

Acknowledgements. This research made use of Lightkurve, a Python package for Kepler and *TESS* data analysis (Lightkurve Collaboration et al. 2018). This paper includes data collected by the *TESS* mission, which are publicly available from the Mikulski Archive for Space Telescopes (MAST). Funding for the *TESS* mission is provided by NASA's Science Mission Directorate. VS and SG acknowledge funding from the German Academic Exchange Service (DAAD PPP USA 57444366) for this project and would like to thank the host institution Texas Tech University for the hospitality. VS was funded by the Deutsche Forschungsgemeinschaft under grant GE2506/9-1. IP was partially funded by the Deutsche Forschungsgemeinschaft under grant GE2506/12-1 and by the UK's Science and Technology Facilities Council (STFC), grant ST/T000406/1. TK acknowledges support from the National Science Foundation through grant AST #2107982, from NASA through grant 80NSSC22K0338 and from STScI through grant HST-GO-16659.002-A. BNB was supported by the National Science Foundation grant AST-1812874. We thank Uli Heber for comments on the manuscript. We thank Andreas Irrgang for the development of the SED fitting tool and making it available to us.

References

- Afşar, M. & Ibanoglu, C. 2008, MNRAS, 391, 802
 Althaus, L. G., Miller Bertolami, M. M., & Córscico, A. H. 2013, A&A, 557, A19
 Astropy Collaboration, Price-Whelan, A. M., Sipőcz, B. M., et al. 2018, AJ, 156, 123
 Astropy Collaboration, Robitaille, T. P., Tollerud, E. J., et al. 2013, A&A, 558, A33

- Baran, A. S., Østensen, R. H., Heber, U., et al. 2021a, *MNRAS*, 503, 2157
- Baran, A. S., Sahoo, S. K., Sanjayan, S., & Ostrowski, J. 2021b, *MNRAS*
- Barlow, B. N., Corcoran, K. A., Parker, I. M., et al. 2022, *ApJ*, 928, 20
- Barlow, B. N., Kilkeny, D., Drechsel, H., et al. 2013, *MNRAS*, 430, 22
- Bell, K. J., Kosakowski, A., Kilic, M., et al. 2019, *Research Notes of the American Astronomical Society*, 3, 81
- Bloemen, S., Marsh, T. R., Østensen, R. H., et al. 2011, *MNRAS*, 410, 1787
- Brown, W. R., Beers, T. C., Wilhelm, R., et al. 2008, *AJ*, 135, 564
- Capitanio, L., Lallement, R., Vergely, J. L., Elyajouri, M., & Monreal-Ibero, A. 2017, *A&A*, 606, A65
- Chen, A., O'Donoghue, D., Stobie, R. S., et al. 1995, *MNRAS*, 275, 100
- Copperwheat, C. M., Morales-Rueda, L., Marsh, T. R., Maxted, P. F. L., & Heber, U. 2011, *MNRAS*, 415, 1381
- Dorman, B., Rood, R. T., & O'Connell, R. W. 1993, *APJ*, 419, 596
- Drechsel, H., Heber, U., Napiwotzki, R., et al. 2001, *A&A*, 379, 893
- Drilling, J. S. 1985, *ApJ*, 294, L107
- Edelmann, H., Heber, U., Altmann, M., Karl, C., & Lisker, T. 2005, *A&A*, 442, 1023
- Edelmann, H., Heber, U., Hagen, H. J., et al. 2003, *A&A*, 400, 939
- For, B. Q., Green, E. M., Fontaine, G., et al. 2010, *ApJ*, 708, 253
- Gaia Collaboration, Brown, A. G. A., Vallenari, A., et al. 2018, *A&A*, 616, A1
- Gaia Collaboration, Brown, A. G. A., Vallenari, A., et al. 2021, *A&A*, 649, A1
- Ge, H., Tout, C. A., Chen, X., et al. 2022, *arXiv e-prints*, arXiv:2205.14256
- Geier, S. 2020, *A&A*, 635, A193
- Geier, S., Heber, U., Kupfer, T., & Napiwotzki, R. 2010, *A&A*, 515, A37
- Geier, S., Hirsch, H., Tillich, A., et al. 2011a, *A&A*, 530, A28
- Geier, S., Marsh, T. R., Wang, B., et al. 2013, *A&A*, 554, A54
- Geier, S., Napiwotzki, R., Heber, U., & Nelemans, G. 2011b, *A&A*, 528, L16
- Geier, S., Østensen, R. H., Heber, U., et al. 2014, *A&A*, 562, A95
- Geier, S., Østensen, R. H., Nemeth, P., et al. 2017, *A&A*, 600, A50
- Geier, S., Raddi, R., Gentile Fusillo, N. P., & Marsh, T. R. 2019, *A&A*, 621, A38
- Gray, D. F. 2005, *The Observation and Analysis of Stellar Photospheres*
- Han, Z., Podsiadlowski, P., Maxted, P. F. L., & Marsh, T. R. 2003, *MNRAS*, 341, 669
- Han, Z., Podsiadlowski, P., Maxted, P. F. L., Marsh, T. R., & Ivanova, N. 2002, *MNRAS*, 336, 449
- Heber, U. 2009, *ARA&A*, 47, 211
- Heber, U. 2016, *PASP*, 128, 082001
- Heber, U., Drechsel, H., Østensen, R., et al. 2004, *A&A*, 420, 251
- Heber, U., Irrgang, A., & Schaffenroth, J. 2018, *Open Astronomy*, 27, 35
- Hillwig, T. C., Frew, D. J., Reindl, N., et al. 2017, *AJ*, 153, 24
- Howell, S. B., Sobek, C., Haas, M., et al. 2014, *PASP*, 126, 398
- Irrgang, A., Geier, S., Heber, U., et al. 2021, *A&A*, 650, A102
- Ivanova, N., Justham, S., Chen, X., et al. 2013, *A&A Rev.*, 21, 59
- Jeffery, C. S. & Ramsay, G. 2014, *MNRAS*, 442, L61
- Kawka, A., Vennes, S., Németh, P., Kraus, M., & Kubát, J. 2010, *MNRAS*, 408, 992
- Kawka, A., Vennes, S., O'Toole, S., et al. 2015, *MNRAS*, 450, 3514
- Kilkeny, D., Koen, C., & Worters, H. 2010, *MNRAS*, 404, 376
- Kilkeny, D., O'Donoghue, D., Worters, H. L., et al. 2015, *MNRAS*, 453, 1879
- Kilkeny, D. & Stone, L. E. 1988, *MNRAS*, 234, 1011
- Kilkeny, D., Worters, H. L., O'Donoghue, D., et al. 2016, *MNRAS*, 459, 4343
- Koen, C. 2009, *MNRAS*, 395, 979
- Koen, C., O'Donoghue, D., Kilkeny, D., Stobie, R. S., & Saffer, R. A. 1999, *MNRAS*, 306, 213
- Krzyszinski, J. & Balona, L. A. 2022, *arXiv e-prints*, arXiv:2204.01604
- Kupfer, T., Bauer, E. B., Burdge, K. B., et al. 2019, *ApJ*, 878, L35
- Kupfer, T., Bauer, E. B., Burdge, K. B., et al. 2020a, *ApJ*, 898, L25
- Kupfer, T., Bauer, E. B., Marsh, T. R., et al. 2020b, *ApJ*, 891, 45
- Kupfer, T., Bauer, E. B., van Roestel, J., et al. 2022, *ApJ*, 925, L12
- Kupfer, T., Geier, S., Heber, U., et al. 2015, *A&A*, 576, A44
- Kupfer, T., Ramsay, G., van Roestel, J., et al. 2017a, *ApJ*, 851, 28
- Kupfer, T., van Roestel, J., Brooks, J., et al. 2017b, *ApJ*, 835, 131
- Lallement, R., Vergely, J.-L., Valette, B., et al. 2014, *A&A*, 561, A91
- Lamontagne, R., Demers, S., Wesemael, F., Fontaine, G., & Irwin, M. J. 2000, *AJ*, 119, 241
- Latour, M., Fontaine, G., & Green, E. 2014, in *Astronomical Society of the Pacific Conference Series*, Vol. 481, 6th Meeting on Hot Subdwarf Stars and Related Objects, ed. V. van Grootel, E. Green, G. Fontaine, & S. Charpinet, 91
- Lei, Z., Zhao, J., Németh, P., & Zhao, G. 2018, *ApJ*, 868, 70
- Lightkurve Collaboration, Cardoso, J. V. d. M., Hedges, C., et al. 2018, *Lightkurve: Kepler and TESS time series analysis in Python*, *Astrophysics Source Code Library*
- Lomb, N. R. 1976, *Ap&SS*, 39, 447
- Lynas-Gray, A. E. 2021, *Frontiers in Astronomy and Space Sciences*, 8, 19
- Maxted, P. F. L., Heber, U., Marsh, T. R., & North, R. C. 2001, *MNRAS*, 326, 1391
- Menzies, J. W. & Marang, F. 1986, in *IAU Symposium*, Vol. 118, *Instrumentation and Research Programmes for Small Telescopes*, ed. J. B. Hearnshaw & P. L. Cottrell, 305
- Mickaelian, A. M. 2008, *AJ*, 136, 946
- Möller, L. 2021
- Morales-Rueda, L., Maxted, P. F. L., Marsh, T. R., Kilkeny, D., & O'Donoghue, D. 2005, in *Astronomical Society of the Pacific Conference Series*, Vol. 334, 14th European Workshop on White Dwarfs, ed. D. Koester & S. Moehler, 333
- Németh, P., Kawka, A., & Vennes, S. 2012, *MNRAS*, 427, 2180
- O'Donoghue, D., Kilkeny, D., Koen, C., et al. 2013, *MNRAS*, 431, 240
- Orosz, J. A. & Wade, R. A. 1999, *MNRAS*, 310, 773
- Østensen, R. H., Geier, S., Schaffenroth, V., et al. 2013, *A&A*, 559, A35
- Østensen, R. H., Green, E. M., Bloemen, S., et al. 2010a, *MNRAS*, 408, L51
- Østensen, R. H., Green, E. M., Bloemen, S., et al. 2010b, *MNRAS*, 408, L51
- Østensen, R. H., Oreiro, R., Solheim, J. E., et al. 2010c, *A&A*, 513, A6
- Pawar, T. 2020
- Pelisoli, I., Neunteufel, P., Geier, S., et al. 2021, *Nature Astronomy*, 5, 1052
- Pelisoli, I., Vos, J., Geier, S., Schaffenroth, V., & Baran, A. S. 2020, *A&A*, 642, A180
- Penoyre, Z., Belokurov, V., & Evans, N. W. 2022, *MNRAS*, 513, 2437
- Pribulla, T., Dimitrov, D., Kjurkchieva, D., et al. 2013, *Information Bulletin on Variable Stars*, 6067, 1
- Ratzloff, J. K., Barlow, B. N., Kupfer, T., et al. 2019, *ApJ*, 883, 51
- Ratzloff, J. K., Barlow, B. N., Németh, P., et al. 2020a, *ApJ*, 890, 126
- Ratzloff, J. K., Kupfer, T., Barlow, B. N., et al. 2020b, *ApJ*, 902, 92
- Reed, M. D., Kawaler, S. D., Zola, S., et al. 2004, *MNRAS*, 348, 1164
- Reed, M. D., Yeager, M., Vos, J., et al. 2020, *MNRAS*, 492, 5202
- Ricker, G. R., Winn, J. N., Vanderspek, R., et al. 2015, *Journal of Astronomical Telescopes, Instruments, and Systems*, 1, 014003
- Rodríguez-López, C., Ulla, A., & Garrido, R. 2007, *MNRAS*, 379, 1123
- Sahoo, S. K., Baran, A. S., Sanjayan, S., & Ostrowski, J. 2020, *MNRAS*, 499, 5508
- Scargle, J. D. 1982, *ApJ*, 263, 835
- Schaffenroth, V., Barlow, B. N., Geier, S., et al. 2019, *A&A*, 630, A80
- Schaffenroth, V., Casewell, S. L., Schneider, D., et al. 2021, *MNRAS*, 501, 3847
- Schaffenroth, V., Classen, L., Nagel, K., et al. 2014a, *A&A*, 570, A70
- Schaffenroth, V., Geier, S., Drechsel, H., et al. 2013, *A&A*, 553, A18
- Schaffenroth, V., Geier, S., Heber, U., et al. 2018, *A&A*, 614, A77
- Schaffenroth, V., Geier, S., Heber, U., et al. 2014b, *A&A*, 564, A98
- Schindewolf, M., Levitan, D., Heber, U., et al. 2015, *A&A*, 580, A117
- Silvotti, R., Østensen, R. H., Bloemen, S., et al. 2012, *MNRAS*, 424, 1752
- Vos, J., Németh, P., Vučković, M., Østensen, R., & Parsons, S. 2018, *MNRAS*, 473, 693
- Vučković, M., Aerts, C., Østensen, R., et al. 2007, *A&A*, 471, 605
- Vučković, M., Bloemen, S., & Østensen, R. 2014, in *Astronomical Society of the Pacific Conference Series*, Vol. 481, 6th Meeting on Hot Subdwarf Stars and Related Objects, ed. V. van Grootel, E. Green, G. Fontaine, & S. Charpinet, 259
- Vučković, M., Østensen, R. H., Aerts, C., et al. 2009, *A&A*, 505, 239
- Vučković, M., Østensen, R. H., Németh, P., Bloemen, S., & Pápics, P. I. 2016, *A&A*, 586, A146

Appendix A: Parameters of the close sdB binaries in TESS

Table A.1: Atmospheric and absolute parameters of the sdB binaries with spectroscopic parameters and with space-based light curves determined by spectroscopy and spectral energy distribution fitting together with the *Gaia* parallax.

| target | $T_{\text{eff,spec}}$ [K] | $\log g_{\text{spec}}$ [cgs] | $T_{\text{eff,sed}}$ [K] | M_{sed} [M_{\odot}] | L_{sed} [L_{\odot}] | R_{sed} [R_{\odot}] |
|---------------------------------|------------------------------|---------------------------------|---|---|---|--|
| Reflection effect systems | | | | | | |
| KPD2215+5037 | 29600 ± 1000 | 5.64 ± 0.10 | 27000 ⁺⁷⁰⁰⁰ ₋₆₀₀₀ | 0.445 ^{+0.063} _{-0.055} | 19.9 ^{+1.9} _{-1.7} | 0.170 ^{+0.005} _{-0.005} |
| JL82 | 26500 ± 500 | 5.22 ± 0.1 | 26000 ⁺⁵⁰⁰ ₋₆₀₀ | 0.294 ^{+0.04} _{-0.034} | 21 ^{+1.9} _{-2.0} | 0.222 ^{+0.006} _{-0.006} |
| HE0230-4323 | 31552 ± 500 | 5.60 ± 0.07 | 34000 ⁺⁸⁰⁰⁰ ₋₅₀₀₀ | 0.635 ^{+0.118} _{-0.094} | 40 ⁺⁶ ₋₅ | 0.211 ^{+0.014} _{-0.012} |
| V1405Ori | 35100 ± 800 | 5.66 ± 0.11 | 27000 ⁺²³⁰⁰ ₋₂₇₀₀ | 0.44 ^{+0.06} _{-0.055} | 36 ⁺⁵ ₋₅ | 0.166 ^{+0.006} _{-0.006} |
| Feige48 | 29850 ± 500 | 5.46 ± 0.05 | 28500 ⁺²⁵⁰⁰ ₋₁₈₀₀ | 0.47 ^{+0.064} _{-0.059} | 32.2 ⁺³ _{-2.8} | 0.213 ^{+0.007} _{-0.007} |
| GALEXJ2205-3141 | 28150 ± 500 | 5.68 ± 0.10 | 26800 ⁺¹¹⁰⁰ ₋₁₀₀₀ | 0.597 ^{+0.078} _{-0.074} | 20.9 ^{+2.0} _{-1.8} | 0.186 ^{+0.005} _{-0.005} |
| PHL457 | 26500 ± 1100 | 5.38 ± 0.12 | 24600 ⁺¹²⁰⁰ ₋₇₀₀ | 0.316 ^{+0.048} _{-0.042} | 16.1 ^{+1.9} _{-1.8} | 0.191 ^{+0.008} _{-0.008} |
| KBS13 | 29700 ± 500 | 5.70 ± 0.05 | 0.472 ^{+0.062} _{-0.057} | 18.2 ^{+1.6} _{-1.5} | 0.162 ^{+0.004} _{-0.004} | |
| CPD-64481 | 27500 ± 500 | 5.60 ± 0.05 | 26500 ⁺¹²⁰⁰ ₋₅₀₀ | 0.437 ^{+0.057} _{-0.050} | 15.7 ^{+1.3} _{-1.3} | 0.1748 ^{+0.0032} _{-0.0030} |
| GALEXJ0321+4727 | 27990 ± 400 | 5.34 ± 0.07 | - | 0.571 ^{+0.145} _{-0.112} | 36 ⁺⁸ ₋₇ | 0.219 ^{+0.005} _{-0.004} |
| J012022+395059 | 29400 ± 500 | 5.48 ± 0.05 | 26500 ⁺²¹⁰⁰ ₋₂₁₀₀ | 0.561 ^{+0.136} _{-0.103} | 24 ⁺⁶ ₋₄ | 0.194 ^{+0.019} _{-0.016} |
| PG1329+159 | 29100 ± 900 | 5.62 ± 0.10 | 27400 ⁺¹¹⁰⁰ ₋₁₀₀₀ | 0.694 ^{+0.101} _{-0.088} | 29.8 ^{+3.1} _{-2.9} | 0.215 ^{+0.008} _{-0.008} |
| BPSCS22169-0001 | 39300 ± 500 | 5.600 ± 0.05 | 40000 ⁺⁹⁰⁰⁰ ₋₅₀₀₀ | 0.584 ^{+0.091} _{-0.076} | 87 ⁺⁹ ₋₈ | 0.202 ^{+0.009} _{-0.008} |
| HS2333+3927 | 36500 ± 1000 | 5.70 ± 0.10 | - | 0.578 ^{+0.094} _{-0.088} | 51 ⁺⁷ ₋₆ | 0.177 ^{+0.011} _{-0.010} |
| UVEX0328+5035 | 28500 ± (500) | 5.500 ± (0.05) | - | 0.375 ^{+0.052} _{-0.046} | 19.6 ^{+1.9} _{-1.8} | 0.182 ^{+0.006} _{-0.006} |
| PG1017-086 | 30300 ± 500 | 5.61 ± 0.10 | - | 0.547 ^{+0.168} _{-0.126} | 28 ⁺⁸ ₋₆ | 0.196 ^{+0.025} _{-0.021} |
| EQ Psc | 28700 ± 500 | 5.63 ± 0.05 | 25400 ⁺¹³⁰⁰ ₋₁₃₀₀ | 0.353 ^{+0.048} _{-0.044} | 13.2 ^{+1.3} _{-1.2} | 0.151 ^{+0.005} _{-0.005} |
| HE1318-2111 | 36300 ± 1000 | 5.42 ± 0.1 | 41000 ⁺⁶⁰⁰⁰ ₋₅₀₀₀ | 0.365 ^{+0.064} _{-0.055} | 60 ⁺⁸ ₋₈ | 0.196 ^{+0.012} _{-0.011} |
| GALEXJ09348-2512 ^a | 40800 ± 500 | 5.55 ± 0.05 | 33000 ⁺¹²⁰⁰⁰ ₋₆₀₀₀ | 0.737 ^{+0.176} _{-0.143} | 133 ⁺³⁰ ₋₂₆ | 0.241 ^{+0.023} _{-0.020} |
| EC01578-1743 ^a | 32200 ± 500 | 5.75 ± 0.05 | 30000 ⁺³⁶⁰⁰ ₋₂₄₀₀ | 0.445 ^{+0.062} _{-0.053} | 21.2 ^{+1.9} _{-1.7} | 0.148 ^{+0.005} _{-0.004} |
| TYC5977-517-1 ^a | 35200 ± 500 | 5.69 ± 0.05 | - | 0.462 ^{+0.07} _{-0.065} | 35 ⁺⁴ ₋₄ | 0.162 ^{+0.008} _{-0.007} |
| HW Vir systems | | | | | | |
| AADor | 42000 ± 1000 | 5.460 ± 0.05 | 35700 ⁺²⁸⁰⁰ ₋₂₂₀₀ | 0.464 ^{+0.058} _{-0.052} | 118 ⁺⁸ ₋₈ | 0.206 ^{+0.005} _{-0.005} |
| ATLASJ340 | 40000 ± 1000 | 5.450 ± 0.05 | - | 0.510 ^{+0.098} _{-0.078} | 116 ⁺¹⁶ ₋₁₄ | 0.225 ^{+0.014} _{-0.013} |
| ATLASJ283 | 50000 ± 1000 | 5.600 ± 0.05 | - | 0.511 ^{+0.075} _{-0.064} | 201 ⁺¹⁷ ₋₁₆ | 0.189 ^{+0.008} _{-0.007} |
| 2M1533+3759 | 29200 ± 500 | 5.58 ± 0.05 | - | 0.427 ^{+0.058} _{-0.053} | 20.3 ^{+2.0} _{-1.8} | 0.176 ^{+0.006} _{-0.005} |
| ASAS102322-3737 | 28400 ± 500 | 5.600 ± 0.05 | 27900 ⁺⁴⁴⁰⁰ ₋₂₈₀₀ | 0.469 ^{+0.065} _{-0.056} | 19.1 ^{+1.9} _{-1.6} | 0.181 ^{+0.006} _{-0.005} |
| 2M1938+4603 | 29600 ± 500 | 5.43 ± 0.05 | - | 0.441 ^{+0.058} _{-0.052} | 31.6 ^{+2.7} _{-2.5} | 0.213 ^{+0.006} _{-0.005} |
| BULSC16335 | 31500 ± 500 | 5.70 ± 0.05 | - | 0.437 ^{+0.121} _{-0.094} | 21 ⁺⁶ ₋₅ | 0.156 ^{+0.018} _{-0.016} |
| EC10246-2707 | 28900 ± 500 | 5.64 ± 0.05 | 26700 ⁺²⁹⁰⁰ ₋₂₆₀₀ | 0.500 ^{+0.076} _{-0.067} | 19.8 ^{+2.3} _{-2.0} | 0.178 ^{+0.008} _{-0.007} |
| HWVir | 28500 ± 500 | 5.63 ± 0.05 | 25700 ⁺¹⁹⁰⁰ ₋₁₇₀₀ | 0.42 ^{+0.055} _{-0.050} | 19.9 ^{+1.9} _{-1.7} | 0.190 ^{+0.005} _{-0.005} |
| HS2231+2441 | 28400 ± 500 | 5.39 ± 0.05 | 28800 ⁺²⁰⁰⁰ ₋₁₅₀₀ | 0.312 ^{+0.052} _{-0.043} | 20.6 ^{+2.6} _{-2.3} | 0.189 ^{+0.010} _{-0.009} |
| PG1336-018 | 32800 ± 500 | 5.76 ± 0.05 | 34000 ⁺⁶⁰⁰⁰ ₋₄₀₀₀ | 0.480 ^{+0.070} _{-0.057} | 22.9 ^{+2.3} _{-2.0} | 0.153 ^{+0.005} _{-0.005} |
| J082053+000843 | 25800 ± 300 | 5.52 ± 0.04 | 27600 ⁺¹⁴⁰⁰ ₋₁₂₀₀ | 0.513 ^{+0.103} _{-0.087} | 17.1 ^{+3.0} _{-2.5} | 0.208 ^{+0.017} _{-0.015} |
| HS0705+6700 | 28800 ± 900 | 5.40 ± 0.10 | 28000 ⁺²⁶⁰⁰ ₋₂₂₀₀ | 0.467 ^{+0.075} _{-0.063} | 31 ⁺⁴ ₋₄ | 0.225 ^{+0.011} _{-0.010} |
| J162256+473051 | 29000 ± 600 | 5.65 ± 0.06 | 28800 ⁺²⁸⁰⁰ ₋₂₀₀₀ | 0.308 ^{+0.076} _{-0.05} | 12.1 ^{+2.7} _{-2.0} | 0.139 ^{+0.014} _{-0.011} |
| ATLASJ296 | 25000 ± 500 | 5.45 ± 0.05 | 19300 ⁺²⁰⁰⁰ ₋₁₅₀₀ | 0.399 ^{+0.075} _{-0.067} | 13.8 ^{+2.2} _{-1.9} | 0.199 ^{+0.013} _{-0.012} |
| J192059+372220 | 27500 ± 1000 | 5.40 ± 0.10 | - | 0.476 ^{+0.091} _{-0.076} | 27 ⁺⁵ ₋₄ | 0.230 ^{+0.016} _{-0.014} |
| V2008-1753 | 32800 ± 250 | 5.83 ± 0.04 | - | 0.47 ^{+0.395} _{-0.179} | 14 ⁺¹³ ₋₆ | 0.124 ^{+0.042} _{-0.026} |
| NSVS14256825 | 40000 ± 500 | 5.50 ± 0.05 | - | 0.406 ^{+0.059} _{-0.052} | 82 ⁺⁷ ₋₈ | 0.189 ^{+0.007} _{-0.007} |
| Ellipsoidal and beaming systems | | | | | | |
| KPD1946+4340 | 34200 ± 500 | 5.43 ± 0.10 | - | 0.452 ^{+0.065} _{-0.056} | 61 ⁺⁶ ₋₅ | 0.216 ^{+0.008} _{-0.007} |
| GD687 | 24300 ± 500 | 5.32 ± 0.07 | 27000 ⁺¹⁸⁰⁰ ₋₁₇₀₀ | 0.283 ^{+0.042} _{-0.037} | 11.7 ^{+1.5} _{-1.3} | 0.194 ^{+0.008} _{-0.008} |
| PG0941+280 | 29400 ± 500 | 5.43 ± 0.05 | 30000 ⁺²⁷⁰ ₋₂₀₀ | 0.363 ^{+0.033} _{-0.048} | 25.1 ^{+2.7} _{-2.5} | 0.194 ^{+0.008} _{-0.007} |
| EVR-CB-004 | 41000 ± 200 | 4.55 ± 0.03 | 40000 ⁺³³⁰⁰ ₋₂₈₀₀ | 0.461 ^{+0.104} _{-0.082} | 910 ⁺¹⁹⁰ ₋₁₆₀ | 0.60 ^{+0.06} _{-0.05} |
| GALEXJ0751+0925 | 30620 ± 400 | 5.74 ± 0.10 | 34000 ⁺⁸⁰⁰⁰ ₋₆₀₀₀ | 0.368 ^{+0.082} _{-0.046} | 14.6 ^{+1.4} _{-1.3} | 0.136 ^{+0.005} _{-0.004} |
| PG1043+760 | 27600 ± 800 | 5.39 ± 0.10 | 28000 ⁺²¹⁰⁰ ₋₄₀₀₀ | 0.289 ^{+0.038} _{-0.036} | 17 ^{+1.6} _{-1.6} | 0.180 ^{+0.005} _{-0.005} |
| EVR-CB-001 | 18500 ± 500 | 4.96 ± 0.04 | 19900 ⁺²⁹⁰⁰ ₋₂₂₀₀ | 0.294 ^{+0.036} _{-0.034} | 9.4 ^{+1.2} _{-1.1} | 0.300 ^{+0.007} _{-0.007} |
| KPD0422+5421 | 25000 ± 1500 | 5.40 ± 0.10 | 23100 ⁺¹⁹⁰⁰ ₋₁₇₀₀ | 0.366 ^{+0.048} _{-0.044} | 14.1 ^{+1.4} _{-1.3} | 0.201 ^{+0.005} _{-0.005} |
| HD265435 | 34300 ± 400 | 5.62 ± 0.10 | 26900 ⁺³⁹⁰⁰ ₋₁₃₀₀ | 0.59 ^{+0.17} _{-0.14} | 51 ⁺⁵ ₋₅ | 0.203 ^{+0.007} _{-0.007} |
| CD-3011223 | 29200 ± 400 | 5.66 ± 0.05 | 29000 ⁺⁴⁴⁰⁰ ₋₂₇₀₀ | 0.44 ^{+0.061} _{-0.056} | 17.7 ^{+1.7} _{-1.6} | 0.164 ^{+0.005} _{-0.005} |

| | | | | | | |
|-------------------------|-------------|-------------|--|---|--------------------------------------|--|
| ZTFJ2130+4420 | 42000±300 | 5.77±0.05 | - | 0.378 ^{+0.061} _{-0.053} | 49 ⁺⁸ ₋₇ | 0.134 ^{+0.007} _{-0.007} |
| J113840-003531 | 31200±600 | 5.54±0.09 | 28500 ⁺³³⁰⁰ ₋₁₂₀₀ | 0.501 ^{+0.096} _{-0.078} | 34 ⁺⁶ ₋₅ | 0.201 ^{+0.013} _{-0.013} |
| KIC6614501 | 23700±500 | 5.70±0.10 | - | 0.361 ^{+0.038} _{-0.049} | 5.7 ^{+0.8} _{-0.7} | 0.142 ^{+0.007} _{-0.007} |
| UVO1735+22 | 38000±500 | 5.54±0.05 | 36000 ⁺¹⁶⁰⁰⁰ ₋₇₀₀₀ | 0.48 ^{+0.07} _{-0.061} | 72 ⁺¹⁰ ₋₉ | 0.197 ^{+0.008} _{-0.008} |
| PG1232-136 | 26900±500 | 5.71±0.05 | 27000 ⁺¹⁴⁰⁰ ₋₁₄₀₀ | 0.402 ^{+0.052} _{-0.049} | 10.2 ^{+1.0} _{-0.9} | 0.148 ^{+0.004} _{-0.004} |
| PG0101+039 | 27500±500 | 5.53±0.07 | 26800 ⁺⁶⁰⁰ ₋₇₀₀ | 0.409 ^{+0.033} _{-0.050} | 17.2 ^{+1.6} _{-1.5} | 0.183 ^{+0.005} _{-0.005} |
| GALEXJ234947.7+384440 | 23800±350 | 5.380±0.06 | -+-- | 0.38 ^{+0.05} _{-0.05} | 12.7 ^{+1.2} _{-1.2} | 0.210 ^{+0.004} _{-0.004} |
| PG1512+244 | 29900±900 | 5.74±0.09 | 27700 ⁺¹³⁰⁰ ₋₁₂₀₀ | 0.41 ^{+0.06} _{-0.05} | 14.7 ^{+1.3} _{-1.2} | 0.143 ^{+0.004} _{-0.004} |
| PG1519+640 | 30600±500± | 5.72±0.05 | 27600 ⁺²⁰⁰⁰ ₋₉₀₀ | 0.45 ^{+0.06} _{-0.06} | 18.6 ^{+1.6} _{-1.5} | 0.154 ^{+0.004} _{-0.004} |
| GALEXJ025023.8-040611 | 28300±500 | 5.67±0.10 | 27000 ⁺²³⁰⁰ ₋₂₃₀₀ | 0.47 ^{+0.07} _{-0.06} | 16.5 ^{+1.7} _{-1.5} | 0.166 ^{+0.006} _{-0.006} |
| PG1743+477 | 27600±800 | 5.57±0.10 | 28000 ⁺¹¹⁰⁰ ₋₁₅₀₀ | 0.49 ^{+0.07} _{-0.06} | 19.3 ^{+1.8} _{-1.7} | 0.193 ^{+0.005} _{-0.005} |
| PG1648+536 | 31400±(500) | 5.62±(0.05) | -+-- | 0.46 ^{+0.07} _{-0.06} | 16.9 ^{+2.4} _{-2.2} | 0.176 ^{+0.005} _{-0.005} |
| PG1000+408 | 36400±900 | 5.540±0.10 | 38000 ⁺²³⁰⁰ ₋₁₇₀₀ | 0.65 ^{+0.11} _{-0.09} | 82 ⁺¹⁰ ₋₉ | 0.229 ^{+0.011} _{-0.011} |
| TONS183 | 27600±0.05 | 5.43±0.05 | 26170 ⁺²⁷⁰ ₋₂₅₀ | 0.38 ^{+0.06} _{-0.05} | 20.5 ^{+2.1} _{-1.9} | 0.198 ^{+0.007} _{-0.007} |
| GALEXJ225444.1-551505 | 31070±300 | 5.80±0.05 | 30700 ⁺¹²⁰⁰ ₋₉₀₀ | 0.39 ^{+0.06} _{-0.05} | 14.4 ^{+1.2} _{-1.1} | 0.131 ^{+0.0029} _{-0.0025} |
| PG0133+114 | 29600±900 | 5.66±0.10 | 23700 ⁺¹⁰⁰⁰ ₋₈₀₀ | 0.38 ^{+0.06} _{-0.05} | 15.9 ^{+1.7} _{-1.5} | 0.152 ^{+0.006} _{-0.005} |
| PG0934+186 | 35800±200 | 5.65±0.02 | 31300 ⁺³⁹⁰⁰ ₋₁₉₀₀ | 0.47 ^{+0.08} _{-0.06} | 43 ⁺⁵ ₋₄ | 0.171 ^{+0.007} _{-0.007} |
| CD-24731 | 35400±500 | 5.90±0.05 | 33500 ⁺¹⁰⁰⁰ ₋₅₀₀ | 0.36 ^{+0.05} _{-0.05} | 18 ^{+1.3} _{-1.2} | 0.1128 ^{+0.0022} _{-0.0021} |
| PHL1539 | 35400±500 | 5.500±0.05 | 36000 ⁺¹⁰⁰⁰⁰ ₋₅₀₀₀ | 0.28 ^{+0.05} _{-0.04} | 34 ⁺⁴ ₋₄ | 0.156 ^{+0.007} _{-0.007} |
| PTF1J082340.04+081936.5 | 27000±500 | 5.50±0.05 | 26400 ⁺¹²⁰⁰ ₋₁₂₀₀ | 0.48 ^{+0.09} _{-0.08} | 20.1 ^{+3.3} _{-2.6} | 0.205 ^{+0.013} _{-0.012} |

Notes: spectroscopic parameters can be found in [Kupfer et al. \(2015\)](#) and references therein as well as references in [Table A.4](#)
^a paper II

Table A.2: Atmospheric parameters, luminosities and radii of the reflection effect candidates without known atmospheric parameters determined by SED fitting and *Gaia* parallax.

| target | $T_{\text{eff, sed}}$ [K] | $\log g_{\text{sed, canonical}}$ [cgs] | L_{sed} [L_{\odot}] | R_{sed} [R_{\odot}] |
|-----------------------------|--|---|--|---|
| 2M0748+3042 | 33700 ⁺⁴⁴⁰⁰ ₋₂₉₀₀ | 5.78 | 21 ⁺¹⁴ ₋₉ | 0.150 ^{+0.012} _{-0.015} |
| HE0505-3833 | 26500 ⁺¹⁴⁰⁰ ₋₁₃₀₀ | 5.63 | 13.2 ^{+3.1} _{-2.6} | 0.175 ^{+0.008} _{-0.007} |
| MCT0049-3059 | 24300 ⁺⁷⁰⁰ ₋₅₀₀ | 5.43 | 15.3 ^{+2.2} _{-1.8} | 0.221 ^{+0.010} _{-0.010} |
| TYC4542-482-1 | 16400 ⁺⁷⁹⁰⁰ ₋₂₄₀₀ | 5.15 | 8.7 ^{+2.6} _{-0.165} | 0.305 ^{+0.028} _{-0.052} |
| EC21390-2930 | 29000 ⁺¹²⁰⁰⁰ ₋₅₀₀₀ | 5.38 | 17 ⁺⁴⁷ ₋₁₄ | 0.241 ^{+0.026} _{-0.049} |
| 2MASSJ18424506+6956202 | 37000 ⁺¹²⁰⁰⁰ ₋₉₀₀₀ | 5.7 | 17 ⁺⁶⁷ ₋₁₇ | 0.169 ^{+0.032} _{-0.030} |
| GALEXJ06206-5705 | 31000 ⁺⁷⁰⁰⁰ ₋₅₇₀₀ | 5.65 | 16.7 ^{+20.3} _{-9.75} | 0.176 ^{+0.017} _{-0.024} |
| 2MASSJ06125523+5750507 | 27000 ⁺⁵⁰⁰⁰ ₋₄₀₀₀ | 5.59 | 10.3 ^{+13.1} _{-6.0} | 0.185 ^{+0.026} _{-0.023} |
| EC01578-1743 | 30000 ⁺²⁴⁰⁰ ₋₂₇₀₀ | 5.73 | 14.9 ^{+8.6} _{-5.2} | 0.158 ^{+0.009} _{-0.013} |
| KUV04421+1416 | 25700 ⁺²⁵⁰⁰ ₋₂₆₀₀ | 5.52 | 14 ⁺⁶ ₋₆ | 0.196 ^{+0.013} _{-0.011} |
| GALEXJ01077-6707 | 25200 ⁺¹²⁰⁰ ₋₁₂₀₀ | 5.48 | 15.3 ^{+3.3} _{-2.8} | 0.208 ^{+0.008} _{-0.007} |
| GAIADR2 2333936291513550336 | 26300 ⁺²⁰⁰⁰ ₋₁₉₀₀ | 5.55 | 15 ⁺⁹ ₋₆ | 0.107 ^{+0.03} _{-0.025} |
| GAIADR2 3573130082641947392 | 25700 ⁺¹⁰⁰⁰ ₋₁₀₀₀ | 5.45 | 18.2 ^{+3.5} _{-2.8} | 0.218 ^{+0.01} _{-0.01} |
| GAIADR2 6366169442902410368 | 25000 ⁺¹³⁰⁰ ₋₁₄₀₀ | 5.4 | 18 ⁺⁵ ₋₄ | 0.231 ^{+0.011} _{-0.011} |
| GAIADR2 6724092123091015552 | 29600 ⁺⁴⁵⁰⁰ ₋₂₈₀₀ | 5.35 | 33 ⁺²⁵ ₋₁₅ | 0.248 ^{+0.016} _{-0.025} |
| GAIADR2-2911497105202950400 | 27100 ⁺²⁷⁰⁰ ₋₂₂₀₀ | 5.52 | 17 ⁺⁹ ₋₆ | 0.2 ^{+0.016} _{-0.016} |
| GAIADR2-3040772322279673472 | 26700 ⁺¹²⁰⁰ ₋₁₁₀₀ | 5.3 | 29 ⁺⁷ ₋₆ | 0.256 ^{+0.013} _{-0.013} |
| GAIADR2-5434436383219257472 | 28300 ⁺³⁹⁰⁰ ₋₂₅₀₀ | 5.46 | 22 ⁺¹⁵ ₋₉ | 0.217 ^{+0.015} _{-0.02} |
| GaiaDR2-3040772322279673472 | 26600 ⁺¹⁴⁰⁰ ₋₁₃₀₀ | 5.30 | 28 ⁺⁸ ₋₆ | 0.256 ^{+0.014} _{-0.013} |
| GaiaDR2-2909497952544966272 | 29000 ⁺⁵⁰⁰⁰ ₋₄₀₀₀ | 5.68 | 13 ⁺¹³ ₋₇ | 0.17 ^{+0.014} _{-0.021} |
| GAIADR2 5416091856344970880 | 28300 ⁺³⁶⁰⁰ ₋₂₄₀₀ | 5.6 | 16 ⁺¹¹ ₋₇ | 0.184 ^{+0.016} _{-0.017} |
| GAIADR2 5576826952945841408 | 25800 ⁺²²⁰⁰ ₋₂₁₀₀ | 5.44 | 17 ⁺⁹ ₋₆ | 0.219 ^{+0.019} _{-0.017} |
| CRTSJ064417.6-464020 | 26800 ⁺³¹⁰⁰ ₋₂₄₀₀ | 5.42 | 20 ⁺¹² ₋₈ | 0.225 ^{+0.018} _{-0.018} |
| GAIADR2 5647303827227273088 | 42000 ⁺¹⁴⁰⁰⁰ ₋₅₀₀₀ | 5.7 | 60 ⁺¹⁰⁰ ₋₄₀ | 0.165 ^{+0.028} _{-0.023} |
| GAIADR2 5296462581763471104 | 36000 ⁺¹⁴⁰⁰⁰ ₋₆₀₀₀ | 5.82 | 16 ⁺⁴⁰ ₋₁₃ | 0.146 ^{+0.018} _{-0.027} |
| 2MASSJ08412266+0630294 | 36700 ⁺³⁸⁰⁰ ₋₂₉₀₀ | 5.7 | 37 ⁺²¹ ₋₁₂ | 0.162 ^{+0.014} _{-0.013} |
| SDSSJ075314.03+111240.1 | 27800 ⁺²⁴⁰⁰ ₋₂₁₀₀ | 5.48 | 22 ⁺¹² ₋₈ | 0.212 ^{+0.026} _{-0.023} |
| GAIADR2 3083335826137398400 | 36000 ⁺¹¹⁰⁰⁰ ₋₇₀₀₀ | 5.9 | 15 ⁺³⁵ ₋₁₂ | 0.13 ^{+0.027} _{-0.023} |
| SDSSJ044246.86-071654.4 | 22700 ⁺¹¹⁰⁰ ₋₁₀₀₀ | 5.3 | 15.6 ^{+3.5} _{-2.9} | 0.259 ^{+0.013} _{-0.012} |
| EC02406-6908 | 25100 ⁺²⁰⁰⁰ ₋₂₁₀₀ | 5.52 | 13 ⁺⁶ ₋₄ | 0.197 ^{+0.012} _{-0.011} |
| GALEXJ14019-7513 | 34000 ⁺¹⁴⁰⁰⁰ ₋₆₀₀₀ | 5.7 | 15 ⁺³⁹ ₋₁₂ | 0.16 ^{+0.017} _{-0.03} |
| HE0516-2311 | 25900 ⁺¹⁴⁰⁰ ₋₁₅₀₀ | 5.4 | 21 ⁺⁷ ₋₆ | 0.229 ^{+0.024} _{-0.021} |
| EC23068-4801 | 29900 ⁺³²⁰⁰ ₋₂₂₀₀ | 5.73 | 15 ⁺⁹ ₋₅ | 0.157 ^{+0.014} _{-0.013} |
| GAIADR2-6652952415078798208 | 24100 ⁺⁵³⁰⁰ ₋₃₀₀₀ | 4.6 | 48 ⁺⁶⁰ ₋₂₉ | 0.48 ^{+0.06} _{-0.06} |
| CRTS-J120928.2-435809 | 26000 ⁺²⁶⁰⁰ ₋₂₃₀₀ | 5.4 | 19 ⁺¹¹ ₋₇ | 0.228 ^{+0.021} _{-0.02} |
| GAIADR2-2943004023214007424 | 26300 ⁺²⁴⁰⁰ ₋₂₂₀₀ | 5.46 | 18 ⁺⁹ ₋₆ | 0.214 ^{+0.086} _{-0.076} |
| GAIADR2-5289914135324381696 | 30000 ⁺⁴⁴⁰⁰ ₋₂₈₀₀ | 5.6 | 20 ⁺¹⁶ ₋₉ | 0.183 ^{+0.026} _{-0.022} |
| PG1628+181 | 26000 ⁺¹⁵⁰⁰ ₋₁₄₀₀ | 5.45 | 18 ⁺⁶ ₋₅ | 0.216 ^{+0.015} _{-0.014} |
| J306.3118+58.8522 | 25400 ⁺²⁵⁴⁰⁰ ₋₂₅₀₀ | 5.65 | 10 ⁺⁹ ₋₅ | 0.176 ^{+0.041} _{-0.03} |
| GaiaDR2-2993468995592753920 | 29700 ⁺⁴⁷⁰⁰ ₋₂₉₀₀ | 5.54 | 22 ⁺¹⁹ ₋₁₀ | 0.198 ^{+0.023} _{-0.022} |
| J084.4719-00.8239 | 28400 ⁺²¹⁰⁰ ₋₁₆₀₀ | 5.52 | 21 ⁺⁸ ₋₅ | 0.2 ^{+0.013} _{-0.012} |
| J129.0542-08.0399 | 26700 ⁺²⁴⁰⁰ ₋₂₁₀₀ | 5.37 | 23 ⁺¹³ ₋₈ | 0.237 ^{+0.031} _{-0.025} |
| GaiaDR2-2969438206889996160 | 27700 ⁺³⁸⁰⁰ ₋₂₅₀₀ | 5.3 | 29 ⁺²¹ ₋₁₂ | 0.262 ^{+0.019} _{-0.024} |
| J089.3714-14.1662 | 28000 ⁺⁶⁰⁰⁰ ₋₄₀₀₀ | 5.52 | 16 ⁺¹⁸ ₋₉ | 0.203 ^{+0.019} _{-0.025} |

Table A.3: Classification of *TESS* targets with no variations

| target | period | K_1 | $M_{2,\min}(M_{\text{sdb}} = 0.47 M_{\odot})$ | $M_{2,\min}(M_{\text{sdb}} = 0.4 M_{\odot})$ | signal-to-noise |
|--|---------------|--------|---|--|-----------------|
| White dwarf companions (M dwarf excluded) | | | | | |
| KPD1930+2752 | 0.0950933 | 341 | 0.90 | 0.85 | ell |
| J083006+475150 | 0.1478000000 | 77.00 | 0.14 | 0.12 | 1% |
| GALEXJ0805-1058 | 0.1737030000 | 29.20 | 0.05 | 0.04 | 0.04% |
| J165404+303701 | 0.2535700000 | 126.10 | 0.32 | 0.29 | 0.4% |
| HE0532-4503 | 0.2656000000 | 101.50 | 0.25 | 0.22 | 0.4% |
| KUV16256+4034 | 0.4776000000 | 38.70 | 0.10 | 0.09 | 0.02% |
| GALEXJ0507+0348 | 0.5281270000 | 68.20 | 0.20 | 0.18 | 0.2% |
| PG1247+554 | 0.60274 | 32.20 | 0.09 | 0.08 | 0.01% |
| PG1248+164 | 0.7323200000 | 61.80 | 0.20 | 0.18 | 0.5% |
| PG0849+319 | 0.7450700000 | 66.30 | 0.22 | 0.20 | 0.5% |
| PG1230+052 | 0.8371770000 | 40.40 | 0.13 | 0.11 | 0.1% |
| PG1116+301 | 0.8562100000 | 88.50 | 0.34 | 0.32 | 0.4% |
| PG0918+029 | 0.8767900000 | 80.00 | 0.30 | 0.28 | 0.1% |
| EC12408-1427 | 0.9024300000 | 58.60 | 0.20 | 0.19 | 0.05% |
| PG2331+038 | 1.2049640000 | 93.50 | 0.44 | 0.40 | 0.5% |
| HE1047-0436 | 1.2132500000 | 94.00 | 0.44 | 0.41 | 0.5% |
| HE2150-0238 | 1.3210000000 | 96.30 | 0.48 | 0.44 | 0.3% |
| PG1403+316 | 1.7384600000 | 58.50 | 0.27 | 0.25 | 0.7% |
| V1093Her | 1.7773200000 | 70.80 | 0.35 | 0.33 | 0.3% |
| CPD-201123 | 2.3098 | 43.50 | 0.21 | 0.19 | 0.05% |
| TON245 | 2.5010000000 | 88.30 | 0.58 | 0.54 | 0.5% |
| PG1253+284 | 3.01634 | 24.80 | 0.12 | 0.11 | 0.01% |
| PG0958-073 | 3.1809500000 | 27.60 | 0.14 | 0.12 | 0.7% |
| KIC10553698 | 3.3870000000 | 64.80 | 0.42 | 0.39 | lc |
| J183249+630910 | 5.4000000000 | 62.10 | 0.50 | 0.46 | 0.5% |
| HE1115-0631 | 5.8700000000 | 61.90 | 0.52 | 0.48 | 1% |
| PG0907+123 | 6.1163600000 | 59.80 | 0.51 | 0.47 | 0.2% |
| PG1032+406 | 6.7791000000 | 33.70 | 0.24 | 0.22 | 0.1% |
| Feige108 | 8.7465100000 | 50.20 | 0.46 | 0.43 | 0.5% |
| KIC11558725 | 10.0545000000 | 58.10 | 0.63 | 0.58 | lc |
| KIC7668647 | 14.1742000000 | 38.90 | 0.40 | 0.37 | lc |
| LB1516 | 10.3598000000 | 48.600 | 0.48 | 0.44 | 0.2% |
| PG1619+522 | 15.3578000000 | 35.20 | 0.36 | 0.33 | 0.1% |
| White dwarf companions (minimum mass, ^a Kupfer et al. (2015)) | | | | | |
| J082332+113641 | 0.2070700000 | 169.40 | 0.44 | 0.41 | 3% |
| J172624+274419 ^a | 0.5019800000 | 118.90 | 0.41 | 0.37 | 5% |
| KPD2040+3955 | 1.4828600000 | 94.00 | 0.49 | 0.45 | 3% |
| J002323-002953 ^a | 1.4876000000 | 81.80 | 0.40 | 0.37 | 2% |
| GALEXJ0812+1601 ^a | 5.1000000000 | 51.00 | 0.37 | 0.34 | 1% |
| PG1244+113 ^a | 5.7521100000 | 54.40 | 0.43 | 0.39 | 1% |
| J095238+625818 ^a | 6.9800000000 | 62.50 | 0.58 | 0.54 | 1% |
| PG0940+068 | 8.3300000000 | 61.20 | 0.62 | 0.57 | 0.3% |
| Feige108 ^a | 8.7465100000 | 50.20 | 0.46 | 0.43 | 1% |
| EC20260-4757 | 8.9520000000 | 57.10 | 0.57 | 0.53 | 0.5% |
| PG1110+294 ^a | 9.4152000000 | 58.70 | 0.61 | 0.57 | 1% |
| PG0919+273 ^a | 15.5830000000 | 41.50 | 0.47 | 0.43 | 1% |
| PG0850+170 | 27.8150000000 | 33.50 | 0.45 | 0.42 | 0.1% |
| Undefined companions | | | | | |
| J095101+034757 | 0.4159000000 | 84.40 | 0.23 | 0.21 | 1.5% |
| HE1059-2735 | 0.5556240000 | 87.70 | 0.28 | 0.26 | 1% |
| J150829+494050 | 0.9671640000 | 93.60 | 0.39 | 0.36 | 1% |
| J113241-063652 | 1.0600000000 | 41.10 | 0.14 | 0.13 | 1.5% |
| KPD0025+5402 | 3.5711000000 | 40.20 | 0.23 | 0.21 | 3% |
| PB7352 | 3.6216600000 | 60.80 | 0.40 | 0.37 | 2% |
| TONS135 | 4.1228000000 | 41.40 | 0.25 | 0.23 | 0.5% |
| PG0839+399 | 5.6222000000 | 33.60 | 0.22 | 0.20 | 1% |
| J032138+053840 | 7.4327 | 39.70 | 0.31 | 0.28 | 0.3% |
| PG1558-007 | 10.3495000000 | 42.80 | 0.40 | 0.37 | 0.75% |
| CS1246 | 14.1050000000 | 16.60 | 0.13 | 0.12 | 3% |
| EGB5 | 16.5320000000 | 16.10 | 0.14 | 0.13 | 0.3% |

Table A.4: All confirmed systems with light variations

| TIC number | name | alternative name | RA [deg] | DEC [deg] | reflection effect systems | classification | G [mag] | $B_p - R_p$ [mag] | parallax [mas] | distance [kpc] | G_{abs} [mag] | reduced pm | period [h] | reference ^a |
|------------|-------------------------------|---------------------------|----------|-----------|---------------------------|----------------|-----------|-------------------|----------------|----------------|------------------------|------------|------------|-----------------------------|
| 4491131 | 2M0748+3042 | Ton287 | 117.233 | 30.713 | | sdB | 14.046156 | -0.347797 | 1.334 | 0.750 | 4.672 | 10.473 | 5.53 | Németh et al. (2012) |
| 14081239 | HE0505-3833 | HE0505-3833a | 76.745 | -38.488 | | sdB | 14.145108 | -0.362259 | 1.228 | 0.815 | 4.591 | 8.454 | 7.73 | O'Donoghue et al. (2013) |
| 28762714 | FB0145+363 | | 27.171 | 36.564 | | sd | 15.462710 | -0.194446 | 3.786 | 0.264 | 8.354 | 12.404 | 3.03 | Mickačian (2008) |
| 66398320 | MCT0049-3059 | PHL867 | 12.907 | -30.716 | | sdB | 14.340959 | -0.392432 | 0.907 | 1.102 | 4.130 | 10.141 | 5.83 | Lamontagne et al. (2000) |
| 67423472 | 2M0156+4003 | | 29.005 | 40.056 | | sdB Vp | 11.430020 | -0.347691 | 3.438 | 0.291 | 4.111 | 8.833 | 4.65 | Geier et al. (2019) |
| 103871878 | 2MASSJ2002943+3137190 | | 300.123 | 31.622 | | sd | 15.480430 | 0.090571 | 1.755 | 1.324 | 4.871 | 10.932 | 6.74 | Geier et al. (2019) |
| 122889490 | 2MASSJ18330407+4637053 | | 278.267 | 46.618 | | sd | 15.698741 | -0.312881 | 1.433 | 0.698 | 4.681 | 11.739 | 1.7 | Geier et al. (2019) |
| 137608661 | 2M0943+7831 | | 145.973 | 78.528 | | sdB V+dM | 11.111541 | -0.411697 | 3.899 | 0.256 | 4.066 | 8.485 | 7.21 | Østensen et al. (2010c) |
| 138025887 | 2MASSJ05545291+7745425 | | 88.72 | 77.762 | | sdB | 15.808988 | -0.040666 | 0.816 | 1.226 | 5.367 | 7.348 | 4.06 | Geier et al. (2019) |
| 142785398 | TYC4542-482-1 | | 154.505 | 75.224 | | sd | 12.597594 | -0.237924 | 2.139 | 0.467 | 4.249 | 8.021 | 4.68 | Schafteinnóth et al. (2019) |
| 162128750 | 2MASSJ22035140+3002560 | | 330.964 | 30.049 | | sd | 13.595135 | -0.286156 | 1.417 | 0.706 | 4.353 | 9.129 | 5.92 | Brown et al. (2008) |
| 173295499 | 2MASSJ23063044+4418488 | | 346.627 | 44.314 | | sd | 14.289134 | -0.127421 | 1.606 | 0.623 | 5.318 | 10.536 | 4.22 | Geier et al. (2019) |
| 189585096 | GALEXJ09348-251248 | | 143.701 | -25.213 | | sdB | 13.044951 | -0.422069 | 1.047 | 0.955 | 3.145 | 9.094 | 3.43 | Mickačian (2008) |
| 207085743 | JL251 | | 23.053 | -49.561 | | sDO | 14.297598 | -0.350369 | 0.950 | 1.053 | 4.186 | 9.246 | 10.17 | Möller (2021) |
| 209393544 | EC21390-2930 | | 325.487 | -29.275 | | sdB+F | 12.802671 | -0.350432 | 1.677 | 0.596 | 3.926 | 10.106 | 10.1 | Kilkenny et al. (2016) |
| 229751806 | 2MASSJ18424506+6956202 | | 280.688 | 69.939 | | sdB | 15.237090 | -0.344561 | 0.619 | 1.616 | 4.194 | 8.622 | 8.08 | Edelmann et al. (2003) |
| 240946701 | 2MASSJ01135301+5005132 | | 18.471 | 50.087 | | sd | 14.954076 | -0.093790 | 1.021 | 0.979 | 5.000 | 7.641 | 7.44 | Geier et al. (2019) |
| 258826647 | HS1909+7004 | | 287.227 | 70.159 | | sdB | 15.478670 | -0.279844 | 0.416 | 2.403 | 3.575 | 8.362 | 8.49 | Østensen et al. (2010c) |
| 259257018 | 2MASSJ0023129+4253099 | | 0.63 | 42.886 | | sd | 14.322986 | -0.226666 | 0.926 | 1.080 | 4.156 | 6.193 | 3.74 | Geier et al. (2019) |
| 260369118 | GALEXJ06206-5705 | | 95.161 | -57.094 | | sDO B | 14.669856 | -0.341110 | 0.869 | 1.151 | 4.365 | 8.955 | 6.01 | Geier et al. (2017) |
| 270491267 | 2M1529+7011 | | 232.36 | 70.198 | | sd | 12.444365 | -0.359034 | 1.981 | 0.505 | 3.929 | 9.543 | 4.79 | Mickačian (2008) |
| 279373920 | TYC4470-864-1 | | 324.573 | 72.186 | | sd | 11.331290 | -0.289723 | 1.460 | 0.685 | 2.152 | 5.231 | 11.24 | Geier et al. (2019) |
| 312220636 | 2MASSJ05534886+3256017 | | 88.454 | 32.934 | | sdB | 14.134800 | -0.058189 | 1.460 | 0.685 | 4.956 | 8.035 | 8.48 | Leit et al. (2018) |
| 322550178 | 2MASSJ06125523+5750507 | | 93.23 | 37.848 | | sd | 15.785784 | -0.236645 | 0.609 | 1.641 | 4.710 | 8.712 | 3.09 | Geier et al. (2019) |
| 333419799 | 2MASSJ23354250+3944269 | | 353.927 | 39.741 | | sdB+dM | 14.565003 | -0.288353 | 0.848 | 1.179 | 4.207 | 7.031 | 4.12 | Heber et al. (2004) |
| 409644971 | GALEXJ175340.57-500741.80 | | 268.419 | -50.128 | | sdB+F7V | 12.893204 | 0.441393 | 1.249 | 0.801 | 3.375 | 8.460 | 2.18 | Németh et al. (2012) |
| 423761655 | EC01578-1743 | | 30.055 | -17.479 | | sdB | 12.023732 | -0.364106 | 3.510 | 0.285 | 4.750 | 10.262 | 6.19 | Kilkenny et al. (2016) |
| 436579904 | KUV04421+1416 | | 71.237 | 14.364 | | sDB Vp | 14.948787 | 0.367522 | 1.441 | 0.694 | 5.742 | 9.106 | 9.54 | Koen et al. (1999) |
| 466277784 | GALEXJ20228-6525 | | 305.713 | -65.423 | | sdB | 13.283801 | -0.328036 | 1.662 | 0.602 | 4.387 | 9.105 | 14.37 | O'Donoghue et al. (2013) |
| 52078744 | GALEXJ01077-6707 | | 16.941 | -17.128 | | sdB | 13.915939 | -0.254942 | 1.397 | 0.716 | 4.642 | 10.325 | 23.67 | Kilkenny et al. (2016) |
| 1672501769 | GAIA DR2 5266468802206471296 | | 97.502 | -71.894 | | sd | 14.247365 | -0.242032 | 1.089 | 0.919 | 4.432 | 8.590 | 3.83 | Geier et al. (2019) |
| 268728844 | GAIA DR2 2208678999172871424 | | 347.643 | 65.009 | | sd | 14.509069 | 0.117362 | 1.366 | 0.732 | 5.268 | 9.915 | 4.89 | Geier et al. (2019) |
| 274949947 | WISEJ003429.0+733329 | | 8.621 | 73.558 | | sd | 14.594332 | 0.087897 | 1.293 | 0.773 | 5.153 | 8.538 | 7.01 | Geier et al. (2019) |
| 202121532 | LAMOSTJ01655.34+511349.7 | | 4.230 | 51.230 | | sd | 16.327900 | -0.195572 | 0.468 | 2.136 | 4.680 | 10.442 | 6.50 | Geier et al. (2019) |
| 122889490 | GAIA DR2 211860752201.5143936 | | 278.267 | 46.618 | | sd | 15.698741 | -0.312881 | 1.433 | 0.698 | 4.681 | 11.739 | 1.70 | Geier et al. (2019) |
| 360026652 | J194649.77+395937.3 | | 296.708 | 39.994 | | sd | 14.381372 | -0.156038 | 0.836 | 1.196 | 3.993 | 10.387 | 10.83 | Geier et al. (2019) |
| 96951246 | J074.5735+30.5930 | | 8.422 | 30.593 | | sd | 15.701506 | 0.311461 | 0.951 | 1.052 | 5.592 | 10.930 | 3.82 | Geier et al. (2019) |
| 202836039 | GAIA DR2 391484413605892096 | | 77.542 | 49.670 | | sd | 16.094658 | -0.179298 | 0.511 | 1.958 | 4.635 | 8.911 | 6.74 | Geier et al. (2019) |
| 367014246 | J077.5424+30.1127 | | 304.270 | 30.113 | | sd | 15.741088 | 0.230632 | 0.869 | 1.150 | 5.437 | 7.727 | 2.75 | Geier et al. (2019) |
| 295895179 | J04.2697+53.7150 | | 109.919 | 53.715 | | sd | 16.325329 | 0.030304 | 0.635 | 1.574 | 5.340 | 9.917 | 5.11 | Geier et al. (2019) |
| 5051080 | TYC5977-517-1 | | 109.919 | -21.889 | | sdB | 12.131400 | -0.357847 | 2.822 | 0.354 | 4.384 | 9.293 | 3.45 | Geier et al. (2019) |
| 12379252 | GAIA DR2 2333936291513550336 | TonS138 | 001.290 | -26.530 | | sdB | 15.990884 | -0.372682 | 0.461 | 2.168 | 4.311 | 7.843 | 6.36 | Sahoo et al. (2020) |
| 386644511 | GAIA DR2 35731.30082641947392 | PG1145-135 | 177.050 | -13.770 | | sdB | 14.255842 | -0.338502 | 0.986 | 1.014 | 4.225 | 9.982 | 12.57 | Sahoo et al. (2020) |
| 2651244418 | GAIA DR2 6366169442902410368 | JL24 | 293.905 | -76.804 | | sdB | 15.260036 | 0.011702 | 0.798 | 1.253 | 4.771 | 10.978 | 5.02 | Sahoo et al. (2020) |
| 86141703 | GAIA DR2 6724092123091015552 | | 271.718 | -43.559 | | sd | 13.453639 | -0.198243 | 1.300 | 0.769 | 4.023 | 10.064 | 4.28 | Sahoo et al. (2020) |
| 37004041 | GAIA DR2 2911497105202950400 | | 090.1499 | -25.198 | | sd | 15.138751 | -0.341063 | 0.673 | 1.483 | 4.283 | 8.304 | 6.80 | Sahoo et al. (2020) |
| 631113578 | GAIA DR2 2921050693020996864 | | 104.606 | -25.415 | | sd | 11.487005 | 0.229303 | 2.693 | 0.371 | 3.638 | 5.793 | 11.65 | Sahoo et al. (2020) |
| 32302937 | GAIA DR2 3040772322279673472 | | 117.391 | -09.096 | | sd | 14.247949 | -0.293413 | 0.849 | 1.177 | 3.893 | 7.644 | 6.28 | Sahoo et al. (2020) |
| 73238638 | GAIA DR2 3083216116810048768 | J08032076-0039394 | 120.837 | -00.661 | | sd | 15.307982 | -0.394972 | 0.471 | 2.121 | 3.675 | 7.652 | 3.30 | Sahoo et al. (2020) |
| 170310610 | GAIA DR2 54344.36383219257472 | | 151.133 | -35.062 | | sd | 14.031923 | -0.268618 | 1.100 | 0.909 | 4.239 | 9.303 | 19.51 | Sahoo et al. (2020) |
| 775878600 | GAIA DR2 5561999385810491264 | | 102.726 | -44.265 | | sd | 15.300258 | -0.260799 | 1.035 | 0.966 | 5.375 | 12.533 | 4.24 | Sahoo et al. (2020) |
| 1036670762 | GAIA DR2 5878353036051735424 | | 218.251 | -61.355 | | sd | 15.063677 | 0.222188 | 1.478 | 0.676 | 5.912 | 9.258 | 7.26 | Sahoo et al. (2020) |
| 4161582 | GAIA DR2 880252005422941440 | LAMOSTJ073756.25+311646.5 | 114.484 | +31.282 | | sdB | 13.553999 | -0.257770 | 1.289 | 0.776 | 4.105 | 10.202 | 6.18 | Baran et al. (2021b) |
| 406417817 | GAIA DR2 1831343410431617920 | | 308.210 | +24.1193 | | sd | 14.702023 | -0.069664 | 0.885 | 1.129 | 4.438 | 10.087 | 4.82 | Baran et al. (2021b) |

| | | | | | | | | | | | | | | |
|-----------------------------------|-----------------------|----------|---|---------|----------|-----|-----------|-----------|-------|-------|-------|--------|--------|-----------------------------|
| 455755305 | GALEXJ234947.7+384440 | " | " | 357.449 | +38.745 | sdB | 11.715421 | -0.189247 | 3.872 | 0.258 | 4.655 | 3.698 | 10.38 | Kawka et al. (2010) |
| 229664008 | PG1512+244 | " | " | 228.635 | +24.178 | sdB | 13.176018 | -0.364226 | 2.170 | 0.461 | 4.858 | 11.138 | 30.48 | Morales-Rueda et al. (2005) |
| 137840206 | EC22202-1834 | " | " | 335.742 | -18.320 | sdB | 13.790620 | -0.370770 | 1.195 | 0.837 | 4.177 | 10.120 | 16.92 | Copperwheat et al. (2011) |
| 229805551 | EC21556-5552 | " | " | 329.753 | -55.634 | sdB | 13.103904 | -0.394528 | 2.022 | 0.495 | 4.632 | 6.748 | 20.89 | Copperwheat et al. (2011) |
| 202491630 | PG1519+640 | " | " | 230.130 | +63.869 | sdB | 12.379927 | -0.423141 | 2.734 | 0.366 | 4.564 | 10.382 | 12.97 | Copperwheat et al. (2011) |
| 10932480 | GALEXJ025023.8-040611 | " | " | 042.600 | -04.104 | sdB | 13.002628 | -0.386107 | 2.025 | 0.494 | 4.535 | 10.632 | 15.92 | Németh et al. (2012) |
| 193600962 | PG1743+477 | " | " | 266.110 | +47.696 | sdB | 13.734726 | -0.386953 | 1.293 | 0.773 | 4.293 | 9.162 | 12.03 | Morales-Rueda et al. (2005) |
| 274385041 | PG1648+536 | " | " | 252.499 | +53.525 | sdB | 14.009392 | -0.338769 | 1.172 | 0.853 | 4.354 | 10.726 | 13.02 | Copperwheat et al. (2011) |
| 9376301 | PG1000+408 | " | " | 150.976 | +40.572 | sdB | 13.249913 | -0.509614 | 0.999 | 1.001 | 3.248 | 9.690 | 26.76 | Copperwheat et al. (2011) |
| 66493797 | TONS183 | " | " | 015.323 | -33.713 | sdB | 12.581187 | -0.410837 | 2.048 | 0.488 | 4.138 | 8.605 | 19.87 | Geier et al. (2011a) |
| 220488137 | GALEXJ225444.1-551505 | " | " | 343.686 | -55.252 | sdB | 12.141099 | -0.453845 | 3.384 | 0.296 | 4.788 | 9.584 | 29.25 | Kawka et al. (2015) |
| 346894954 | PG0133+114 | " | " | 024.109 | +11.659 | sdB | 12.275509 | -0.344523 | 3.153 | 0.317 | 4.769 | 9.905 | 29.70 | Morales-Rueda et al. (2005) |
| 91986289 | PG0934+186 | " | " | 144.318 | +18.420 | sdB | 13.075914 | -0.458850 | 1.538 | 0.650 | 4.010 | 9.247 | 97.73 | Copperwheat et al. (2011) |
| 33490778 | CD-24731 | " | " | 025.952 | -24.086 | sdB | 11.684070 | -0.494827 | 4.334 | 0.231 | 4.869 | 11.611 | 138.74 | Geier et al. (2011a) |
| 142875987 | PHL1539 | " | " | 051.643 | -31.062 | sdB | 14.022624 | -0.479381 | 1.076 | 0.930 | 4.181 | 10.142 | 60.11 | Bell et al. (2019) |
| Central stars of planetary nebula | | | | | | | | | | | | | | |
| 342025025 | UUsgc | " | " | 295.543 | +17.0873 | sdO | 14.974704 | 0.284213 | 0.365 | 2.739 | 2.787 | 9.539 | 11.16 | Afşar & İbanoğlu (2008) |
| 423311936 | V477Lyr | " | " | 277.827 | +26.937 | sdO | 14.957651 | -0.229764 | 0.404 | 2.474 | 2.991 | 6.469 | 11.32 | Afşar & İbanoğlu (2008) |
| FF1 | HaTr7 | PN HaTr7 | " | 268.539 | -60.833 | sdO | 14.829035 | -0.306667 | 0.587 | 1.704 | 3.672 | 10.279 | 7.73 | Hillwig et al. (2017) |
| 334382552 | EGB5 | " | " | 122.803 | +10.955 | sdO | 13.775318 | -0.472623 | 1.593 | 0.628 | 4.787 | 10.030 | 396.77 | Geier et al. (2011b) |
| 120596335 | CD-486027 | " | " | 163.669 | -48.785 | sdO | 12.135967 | -0.276526 | 1.226 | 0.816 | 2.579 | 8.616 | 8.57 | Drilling (1985) |

^a Light variation analysis an/or atmospheric parameters or spectral classification